

The ERA5's Diurnal Cycle of Low-Level Clouds Over Western Central Africa During June-September: Dynamic and Thermodynamic Processes.

Atanas Dommo (✉ dmmatanas@gmail.com)

University of Yaoundé 1 <https://orcid.org/0000-0001-8667-4791>

Derbetini A. Vondou

University of Yaoundé 1

Nathalie Philippon

University of Grenoble Alpes

Ryan Eastman

University of Washington

Vincent Moron

Aix Marseille Univ

Noel Aloysius

University of Missouri

Research Article

Keywords: Low clouds, relative humidity, dynamic, thermodynamic

Posted Date: September 29th, 2021

DOI: <https://doi.org/10.21203/rs.3.rs-689885/v1>

License: © ⓘ This work is licensed under a Creative Commons Attribution 4.0 International License.

[Read Full License](#)

1 **Title: The ERA5's diurnal cycle of low-level clouds over Western Central Africa during**
2 **June-September: dynamic and thermodynamic processes.**

3
4 **A. Dommo**

5 Laboratory of Environmental Modeling and Atmospheric Physics, University of Yaoundé 1,
6 Yaoundé, Cameroon, 0000-0001-8667-4791

7 **Derbetini A. Vondou**

8 Laboratory of Environmental Modeling and Atmospheric Physics, University of Yaoundé 1,
9 Yaoundé, Cameroon, 0000-0002-8681-5328

10 **N. Philippon**

11 IGE, University of Grenoble Alpes, CNRS, IRD, Grenoble INP, Grenoble, France, 0000-
12 0003-3519-539X

13 **R. Eastman**

14 Department of Atmospheric Sciences, University of Washington, Seattle, Washington, 0000-
15 0001-8696-4211

16 **V. Moron**

17 Aix Marseille Univ, CNRS, IRD, INRAE, Coll. de France, CEREGE, Aix en Provence,
18 France and IRI, Columbia University, Palisades, NY, USA, 0000-0002-4981-9530

19 **N. Aloysius**

20 Department of Natural Resources, University of Missouri, Columbia, Missouri, USA, 0000-
21 0002-9094-427X

22
23 **Corresponding author:** Atanas DOMMO. Laboratory of Environmental Modelling and
24 Atmospheric Physic (LAMEPA), University of Yaounde 1, Yaoundé, Cameroon
25 Email: dmmatanas@gmail.com

26
27 **Acknowledgements:**

28 Authors thank NASA (National Aeronautics and Space Administration) for providing MODIS
29 low clouds data. They also acknowledge the ECMWF for providing reanalysis (ERA5) data.
30 We are also grateful to Andreas Fink and Peter Knippertz for their helpful contributions.

31 **Abstract**

32 This paper analyzes the diurnal cycle of low cloud cover (LCC) and the atmospheric
33 conditions under which it grows over Western Central Africa during the cloudiest season
34 (June-September). Moderate Resolution Imaging Spectroradiometer (MODIS) observations,
35 Extended Edited Clouds Reports Archive (EECRA) and the fifth generation of reanalysis of
36 the European Centre for Medium Range Weather Forecasts (ECMWF), i.e., ERA5 are used.
37 LCC peaks between 04LT and 07LT and tends to be less dense during the afternoon. The
38 associated dynamic and thermodynamic ERA5 conditions reveal different processes. The
39 strong low level (below 1000 m) southwesterly flow in the evening supplies the region with
40 humidity from the ocean and leads to cloud formation. Relative humidity (RH) tendencies
41 show that temperature contributes to 100% of RH changes : the strong cooling observed after
42 sunset at 19LT increases RH in the area of about 8%/h in the lower layer (below 1000m). The
43 nighttime cooling shows strong cooling rates of about -1.4K/h after sunset till 22 LT, then
44 rates decrease during the night to reach a value of about -0.3K/h between 22LT and 07LT.
45 The cloud formation is mostly related to horizontal air advection, strong convergence in the
46 lower layer and turbulent upwards mixing of moisture, while cooling at the cloud-top helps to
47 maintain the cloud deck once it has formed. During daytime, solar radiation suppressed
48 cooling at the cloud-top, thereafter strong turbulent kinetic energy acts to partly destroy the
49 cloud deck and cloud fraction.

50 **keywords:** Low clouds, relative humidity, dynamic, thermodynamic

51

52

53 **Introduction**

54

55 Low level clouds cover large regions of the Earth's surface. Worldwide, low clouds
56 cover (LCC) approximately 28% of the earth's land surface (Hahn and Warren 2007) and
57 impact earth's surface energy balance (Chen et al. 2000) mostly by decreasing incoming solar
58 radiation at the surface. Low clouds are close to the Earth's surface and therefore exert a
59 relatively small effect on the top of atmosphere outgoing longwave radiation (Stephens and
60 Greenwald 1991; Hartmann et al. 1992). Consequently, LCC produces a strong net cooling at
61 the surface. In general, low clouds form in strong lower tropospheric static stability, in
62 response to either cooling or moistening of the boundary layer (Wood et al. 2012) driven by
63 radiative processes, buoyancy and advection. However, turbulent mixing may be more
64 efficient in many circumstances for generating large scale saturation. Under certain

65 conditions, Garratt (1999) shows that the primary source of turbulence may be vertical shear
66 of horizontal wind or buoyancy flux due to exchange of latent heat release from the surface.
67 Paluch and Lenschow (1991) argue that the exchange with the surface is critically dependent
68 upon the buoyancy of the air immediately close to the surface.

69 The understanding of climatic processes over Central Africa suffers from the
70 unavailability of in situ observations. This holds particularly true for low cloud cover over the
71 region while its misrepresentation in climate models biases temperature and rainfall
72 simulations and projection (Knippertz et al. 2011; Schuster et al. 2013). Most of the studies
73 dedicated to the climate of Central Africa revolve around numerical simulations with the main
74 objectives of evaluating climate models (Mba et al. 2018; Fotso et al. 2016, 2017; Vondou et
75 al. 2017; Sonkoue et al. 2018; Tamoffo et al. 2019a). For instance, Tamoffo et al. (2021) used
76 process-based evaluations to assess the performance of two versions of Rossby Centre
77 Regional Climate Model (RCA4) in simulating rainfall over Congo Basin. The two versions
78 are RCA4 version 1 (RCA4-v1) with strong turbulent mixing and the modified one, RCA4
79 version 4 (RCA4-v4), with reduced turbulent mixing. These authors show that RCA4-v4
80 injects less moisture to the free atmosphere, and thus leads to an anomalous moistening of the
81 lower layers and an increasing LCC. This increasing LCC is more pronounced over West
82 Central Africa (WCA) than over the Congo Basin. Consequently, the surface solar radiation is
83 reduced over WCA, then enhances the surface temperature gradient between WCA and the
84 Congo Basin. Dommo et al. (2018) have produced the first assessment of the mean spatio-
85 temporal evolution of LCC over WCA using a set of satellite data, ground-based observation
86 and reanalysis. These authors find that WCA is mostly covered by low stratiform clouds
87 during the June-September (JJAS) dry season and this LCC is particularly important for forest
88 growth (Philippon et al. 2019). Stratiform low clouds are generally observed in coastal areas
89 (Pilié et al. 1979; Cermak 2012) where they sustain vegetation by lowering temperature and
90 bringing substantial amounts of water. These ecosystems may not be present without LCC
91 (Del-Val et al. 2006; Garcia-Santos et al. 2004). In WCA, LCC extends inland up to around
92 15°E then dissipates just westward of the Congo basin leeward of low-level W-SW winds (i.e.
93 westward of Chaillu Mts, Cristal Mts and Batéké plateaus). The coastal plains approximately
94 between Libreville (Gabon) and Pointe Noire (Congo) and the ocean facing valleys have the
95 largest LCC with a maximum intensity at 04 LT (Dommo et al. 2018). Over hills and
96 plateaus, LCC decreases with a maximum intensity at 10LT. The dissipation of LCC east of
97 15°E may be at least partly due to the foehn effect (Dommo et al. 2018). While this recent
98 study helped to underline the diurnal evolution and spatial extension of low clouds in WCA,

99 until now, very little attention has been paid to these clouds. In WCA, Dommo et al. (2018)
100 haven't produced an in-depth analysis on cloud controlling mechanisms such as
101 thermodynamic (relative humidity change, radiative cooling, heating at the surface) and
102 dynamic (humidity advection and convergence, turbulence, vertical mixing) that control low
103 cloud formation and dissipation at the diurnal scale. This incompleteness in the study of
104 processes driving LCCs formation, maintenance and dissipation is a crucial limitation for
105 climate studies and modeling in WCA, demanding substantial improvements. In SWA, low
106 level clouds form during the night and persists during the following day (Kalthoff et al 2018).
107 They affect the energy balance at the surface and the diurnal cycle of the atmospheric
108 boundary layer (Knippertz et al. 2011, Hannack et al. 2017). Schrage et al. (2007) showed that
109 cloudy nights in Parakou are characterized by strong moisture convergence at 925hPa and a
110 low static stability. In SWA, intensifying nocturnal low-level jets (NLLJ) drive cloud
111 formation (Knippertz et al. 2011, Schrage and Fink 2012, Schuster et al. 2013, Babic et al.
112 2019, Lehou et al. 2020, Alder et al. 2019, Zouzoua et al. 2021). Prior to low- cloud
113 formation, cold air advection -bringing large amounts of humidity- from the sea in addition to
114 strong radiative cooling over land after sunset are the main factors leading to saturation. After
115 formation, the deck is maintained by a well-mixed sub-cloud layer due to vertical shear driven
116 turbulence associated with the intensity of NLLJ. Schuster et al. (2013) shown that in very
117 stable conditions, turbulent energy is dissipated in the area of strong radiative cooling after
118 sunset. Schrage et al. 2007 found that if radiative cooling is anomalously strong, the surface
119 layer can decouple with the lower atmosphere, impeding the cloud formation whereas
120 turbulent fluxes of moisture and heat can support cloud formation depending on vertical
121 stability. Babic et al. (2019a) showed that cooling increases the relative humidity leading to
122 saturation and cloud formation. After sunrise, solar heating at the surface causes positive
123 sensible heat flux and upwards transport of warm air thus deepening the atmospheric
124 boundary layer (ABL) (Babic et al. 2019, Lehou et al. 2020, Alder et al. 2019).

125

126 The main objective of this study is to make a more complete description of atmospheric
127 conditions and processes relevant to the diurnal cycle of low clouds in JJAS in WCA (**Fig 1**),
128 thus deepening the preliminary study of Dommo et al. (2018). We seek to answer the
129 following questions: what the dynamic and thermodynamic conditions under which low
130 clouds grow along the diurnal cycle in WCA during the cloudy dry season (JJAS).
131 Specifically, is turbulence necessary for LCCs formation in WCA ? Up to what degree does
132 turbulence contribute to LCCs formation or dissipation in WCA ? What dominates the relative

133 humidity and advection changes during the diurnal cycle ? What surface conditions are
134 relevant to low cloud formation and dissipation ? Because of the lack of in situ and aircraft
135 measurements in WCA, our analysis is mostly based on ERA5 reanalysis that provides high
136 spatio-temporal datasets and various atmospheric parameters useful to assess the dynamic and
137 thermodynamic conditions relevant for low-cloud formation and dissipation. The paper is
138 organized as follows: in section 2 we make a brief description of the data used and statistical
139 analysis applied on ground and satellite observations and ERA5. Section 3 includes a brief
140 validation of ERA5 low cloud fraction against satellite and ground observations. In section 4,
141 the diurnal cycle of low cloud cover in ERA5 is assessed. Section 5 depicts the atmospheric
142 conditions relevant to the low cloud cover diurnal cycle and we end in section 6 with a
143 conclusion and discussion.

144

145 **1) Data**

146 In this section, we briefly describe and characterize the three cloud products used in
147 this study. The first two are the daily Moderate Resolution Imaging Spectroradiometer
148 (MODIS) Satellite data from National Aeronautic and Space Administration (NASA) and the
149 in-situ observations (Extended Edited Clouds Reports Archive (EECRA) collected from
150 ground-based observations). The last dataset is the fifth generation of reanalysis of the
151 European Centre for Medium Range Weather Forecasts (ECMWF), i.e., ERA5, which is the
152 improved version of ERA Interim. ERA5 reanalysis are used to investigate the atmospheric
153 and thermodynamic conditions under which low clouds grow in WCA, whereas EECRA and
154 satellite observations are used in this study for spatial and diurnal comparisons with ERA5.

155 The topographic aspects of the study area are displayed in **Fig 1**. The region is
156 characterized by moderate topographic elevation (**Fig 1**) with plateaus, coastal plains and
157 valleys. Details about the geographical aspects of the study area can be found in Dommo et al.
158 (2018).

159

160 **2.1 Satellite and observational data of low clouds**

161 **2.1.1 MODIS low clouds cover**

162 MODIS is a key instrument of NASA's Earth Observing System (EOS) on board Terra
163 and Aqua satellites (Sun et al. 2012). With a sun-synchronous polar orbit nearly perpendicular
164 to the equator, both Terra and Aqua satellites offer a daytime and nighttime view of the

165 Earth's surface. Their equator crossing times are 1:30am and 13:30 pm LT for Aqua and
166 10:30am and 22:30pm LT for Terra. MODIS sensor collects data within 36 spectral bands,
167 ranging from 0.4 micrometer to 14.4 micrometer, and provides images at 250m resolution at
168 nadir for two bands, 500m resolution for 5 bands and the remaining 29 bands at 1 km.
169 Sixteen of the 1 km resolution bands cover medium to large infrared wavelengths (3.75-14.2
170 μm). The data used are L3 MODIS daytime, nighttime and daily timescales at $1^\circ \times 1^\circ$ grid
171 point. The level-3 statistics include mean, minimum, maximum, standard deviation and also
172 fraction of cloudy and clear pixels. In the level-3 dataset, statistics of each $1^\circ \times 1^\circ$ gridpoint are
173 derived by subsampling and aggregating every fifth of 1-km near-nadir pixel (Oreopoulos,
174 2005). For this study, both Aqua (MYD08_D3) and Terra (MOD08_D3) daily mean low cloud
175 fraction for the period 2014-2015 at 1 km spatial resolution are combined and account for
176 MODIS low clouds. MODIS low clouds cover is obtained by reprocessing the MODIS
177 (<https://ladsweb.modaps.eosdis.nasa.gov/archive/allData/61/>) day and night cloud mask data
178 using a cloud top temperature (CTT) filter at 0°C . The filter aims to eliminate all observations
179 with CTT below 0°C , given that the study area is a warm area. The cloud mask algorithm
180 (Ackman et al. 1988) uses a series of thresholds applied to 20 of the 36 MODIS bands to
181 identify the presence of clouds and give information on individual cloud test results.

182 **2.1.2 EECRA**

183 The EECRA data used in this study are ground based observations i.e. the type of
184 cloud is determined by a trained observer, based on cloud base height and physical
185 characteristics (www.atmos.washington.edu/CloudMap/). The land-based EECRA data are
186 from 5388 weather stations on land areas spread over all continents, as well as a few stations
187 on Arctic sea ice. EECRA offers a climatology for the 1971-2009 period of different cloud
188 types within the low, middle and high levels of the atmosphere in addition to cloud base
189 height and present weather conditions. Reports from automated weather stations that do not
190 contain cloud information are not included in EECRA database. Several quality controls were
191 applied on raw reports so that inconsistent reports are excluded. Nighttime observations are
192 screened for adequate lunar illuminance (Hahn et al. 1995) to correct underestimation of
193 clouds due to inadequate nighttime illumination of cloud cover. The dataset includes monthly
194 averages, seasonal, multi-year annual averages as well as 3-hourly reports for eight reporting
195 times per day (01, 04, 07, 10, 13, 16, 19, 22LT). For this study, we use 3-hourly low cloud
196 amount for the period JJAS 1971-2009 over the WCA. Low clouds type (their base height is
197 generally below 600m) are as follows: fog, stratus, stratocumulus, cumulus and

198 cumulonimbus; nimbostratus, altocumulus, altostratus for middle clouds and finally
199 cirrostratus, cirrus, cirrocumulus, dense cirrus for high clouds. In EECRA, stratocumulus as
200 well as cumulus and cumulo-nimbus are classified as low clouds because their base height is
201 close to the surface despite a larger vertical extension. The number of reports varies
202 considerably. Then, to avoid bias due to missing records, we selected the 18 stations which
203 provide at least 25% of 3-hourly data during JJAS over the 39-year EECRA span (red
204 triangles on Fig 1). The diurnal cycle is obtained by averaging low clouds amount over each
205 of the eight time steps for JJAS seasons and for the 18 stations.

206 2.2 ERA5 data

207 Within Copernicus Climate Change Services, the European Centre for Medium-range
208 Weather Forecasts (ECMWF) currently produces the Fifth Generation Reanalysis (ERA5)
209 which includes a detailed record of the global atmosphere, land surface and ocean waves from
210 1950 to present. This new reanalysis replaces the previous ERA Interim reanalysis that was
211 launched in 2006. ERA5 is based on the 41r2 cycle of the integrated operational forecasting
212 system (IFS) since 2016. In addition to its high horizontal resolution (31km, compared to
213 75km for ERA-interim), ERA5 also extends to 137 altitude levels (from the surface to 0.01
214 hPa, i.e. 80 km). ERA5 provides hourly data for a large number of atmospheric and oceanic
215 variables and includes uncertainty information for all variables (Hersbach et al. 2018). The
216 IFS relied on a number of prescribed radiation forcings and ocean surface conditions. Based
217 on the number of input parameters
218 (<https://confluence.ecmwf.int/display/CKB/ERA5+data+documentation>) and many new or
219 reprocessed observations, ERA5 is appropriate for climate study (Lei et al. 2020). The use of
220 ERA5 has many advantages: 1) it offers data at the high spatiotemporal resolution which is
221 suitable for regions lacking in situ observation, 2) it offers a wide range of parameters that
222 allow for in-depth study of dynamic and thermodynamic conditions. In addition to different
223 atmospheric parameters provided by ERA5, it also provides cloud variables in 2-D and 3-D
224 dimensions. For our present study, we used hourly data on their native spatial resolution
225 (31kmx31km) for the period 2014-2015. Due to limited computational resources, only two
226 years are chosen for thermodynamic and dynamic analyses. Considering land only pixels over
227 the interested area, the representativeness of the two selected years is checked by computing
228 the diurnal cycle of low clouds fraction for each of the years 1979-2019 (**Fig 2**).

229 Both years 2014 and 2015 are cloudier than normal. The amplitude of the diurnal cycle is
230 almost constant from one year to the other, so the analysis of the diurnal cycle of the above-

231 mentioned years is a good approximation of what may happen on average over WCA. For our
232 present study, low level cloud fraction (3-D and 2-D), total column water vapor and total
233 column liquid water content are extracted for low cloud characteristics. Also, wind (horizontal
234 and vertical components), temperature, relative and specific humidity, cloud liquid water
235 content, net shortwave and longwave radiation, surface latent and sensible heat are used for
236 dynamic and thermodynamic processes. In addition, vertical profiles of moisture convergence
237 and advection, relative humidity changes, cooling and the main contribution to horizontal
238 advection are investigated.

239 3) ERA5 evaluation against MODIS and EECRA

240 Here we compare the mean spatial distribution as well as the diurnal evolution of LCC
241 fraction in ERA5 during JJAS season with MODIS and EECRA over WCA. This will
242 reveal the capability of ERA5 to capture the spatial distribution as well as the diurnal cycle of
243 LCC in WCA. We focus our analysis on the land area 6°S-5°N and 8°E-15°E (**Fig 1**). The
244 LCC spatial distribution is controlled by topography and a rapid decrease in cloud amount is
245 observed eastward from 15°E, corresponding to the downward slopes facing toward the
246 Congo basin (Dommo et al. 2018).

247 3.1) Mean seasonal pattern

248 **Fig 3** displays the mean frequency of LCC over WCA using Terra and Aqua MODIS
249 (hereafter, MODIS) data (**Fig 3a**), ERA5 reanalysis (**Fig 3b**) and EECRA (**Fig 3c**) both for
250 nighttime and daytime. **Fig 3d** displays the mean diurnal cycle of EECRA stations and the
251 corresponding ERA5 pixels. Also presented in **Fig 3** are the spatial averages of four grid-
252 points representing MODIS cloud amount for each crossing time as stated in section 2.1.1. All
253 three products show a local cloud maxima greater than 80% along the Atlantic coast, namely
254 the Cameroonian Coast, Gabon, and almost all of SW Congo, west of Brazzaville (**Fig 1**).
255 There are some substantial differences between the spatial distribution of the three products:
256 both MODIS and EECRA (**Fig 3a & 3c**) show LCC fraction $\geq 65\%$ in almost all parts of
257 our box area whereas ERA5 (**Fig 3b**) struggles to represent low clouds in south East
258 Cameroon and eastern Gabon (their amounts are not greater than 50%). To make comparable
259 estimates with EECRA data, the diurnal cycle is computed by averaging for each time step
260 only the 18 ERA5 pixels close to the EECRA stations (**Fig 1**). **Fig 3d** displays the mean
261 diurnal cycle of low-level clouds from EECRA stations and for the corresponding ERA5 and
262 MODIS pixels. Diurnal cycles of low clouds from EECRA and ERA5 are largely in phase

263 despite some discrepancy from late afternoon to early night. Diurnal cycle amplitude of
264 EECRA is about 15% compared to 35% for ERA5 and 24% for MODIS. The differences
265 among the two products along the diurnal cycle and for each pixel/station are the largest
266 (>20%) in the early night, however this difference decreases from late night (about 10%) to
267 late morning at 10LT (about 4%).

268 In term of amounts, EECRA shows a maximum cloud amount of about 80% at 04 LT and a
269 minimum of about 65% at 22 LT. This maximum remains constant until 10LT. ERA5 shows
270 a maximum (minimum) cloud amount of about 80% (40%) at 10 LT (19 LT) whereas MODIS
271 shows a maximum (minimum) of about 94% (70%) at 10.30 am (22.30 pm). MODIS may
272 have a tendency to overestimate cloud amounts compared to EECRA observations. This is
273 because MODIS clouds are observed from all parts of the MODIS swath, including near
274 edges where the wide sensor view angle biases cloud amount (Maddux et al. 2010).

275 **3.2) Diurnal evolution of the spatial pattern**

276 To compare spatial evolution of ERA5 LCC with that of EECRA along the diurnal
277 cycle, only eight time slots (01, 04, 07, 10, 13, 16, 19, 22LT) are retained for ERA5 analyses.
278 The spatial evolution of LCCs cover along the diurnal cycle as observed in ERA5 is
279 represented in **Fig 4a**. LCC begins forming in the first half of the night at about 22 LT in the
280 high-elevation areas of south Cameroon. Clouds spread progressively along the Gabon coast
281 and continue to grow during the course of the night so that at 07 LT LCCs cover the majority
282 of the area. From 01 LT to 07 LT, LCCs are mostly confined along the west facing slopes
283 with a maximum cloud cover reaching 95%. At 10LT, a north-south gradient of cloud cover is
284 observable. Low clouds start dissipating in south Cameroon and Equatorial Guinea whereas
285 the LCC cover increases in the coastal plains and west facing slopes of Gabon and the SW
286 Republic of Congo, with frequency above 90% until 16 LT. At 16 LT, clouds begin
287 significantly dissipating, even if substantial amounts (55~60%) are still seen at 19LT. **Fig 4b**
288 shows the three hourly spatial distribution of LCCs as observed in EECRA stations. The
289 observed spatial distribution shows that during the diurnal cycle, EECRA low cloud amounts
290 are generally greater than 50% in almost all parts of the green box, except for a few stations in
291 SW Congo republic at 01LT and 22LT showing amounts between 40 and 50%. Also
292 observed in **Fig 4b** is the north-south dissipation of low clouds from 16LT to 22LT. All these
293 features are also observed in ERA5 even if there are some differences between the two
294 products during the diurnal cycle. For instance, from 10 LT, LCCs diminish for coastal

295 EECRA stations (**Fig 4b**) while it is not observed in ERA5, but the frequency stays over 60%
296 in EECRA. Furthermore, LCCs in EECRA are always present over south west Gabon with a
297 maximum cloud cover greater than 90%, whereas in ERA5 amounts are barely above 70% in
298 this area between 19LT and 22LT.

299 Despite an underestimation of low clouds by ERA5 with respect to spatial frequencies and
300 throughout the diurnal cycle, ERA5 does show reasonable agreement with ground-based
301 observations. The spatial pattern of LCCs in ERA5 also matches well with CALIOP and
302 SAFNWC retrievals (see Fig 2a,b in Dommo et al. 2018). The LCCs underestimation in
303 ERA5 is likely due to the weakly incorporated land assimilation system, combining in-situ
304 and satellite observations (Hersbach et al. 2018). The relative agreement between satellite
305 observations and ERA5 low level clouds has already been drawn in West Africa (Danso et al.
306 2019) and over Tibetan plateau and eastern China (Lei et al. 2020). So, because of ERA5
307 improved spatial/temporal resolution, the following analysis will be made using ERA5
308 variables to picture out low-level cloud diurnal cycle characteristics and thermodynamic
309 processes.

310 Clouds form when air becomes saturated with respect to liquid water. Under certain
311 conditions, water vapor condenses into some atmospheric particles to form clouds. Then, time
312 series of total column cloud liquid water content (LWP hereafter) together with total column
313 water vapor (TWV) are shown in **Fig 4c**. The diurnal cycle of TWV varies very much
314 slightly. The minimum of LWP is observed at 21LT. Thereafter and during the course of the
315 night, there is an increase of LWP with a first maximum observed at 05LT then a second one
316 at 10LT, probably in links with clouds thickening and spreading over the region. During
317 daytime, LWP decreases strongly (together with LCCs dissipation) to reach its daily
318 minimum. The features observed in this figure suggest that different atmospheric mechanisms
319 are at play to explain the LCCs diurnal cycle. These aspects are explored in the following
320 section. In the following analyses, only land pixels are considered within the green box in **Fig**
321 **4a** as processes driving low clouds may be different on land and on sea. To account only for
322 the cloudiest areas, only land pixels within the green box which recorded on average at least
323 80% of low clouds at 07LT are considered. This threshold also enables to reduce biases due to
324 spatial heterogeneity as the processes driving low cloud cover may be different over the coast,
325 windward slopes and plateaus.

326

327 **4) Atmospheric conditions associated with the diurnal cycle of LCCs**

328 In this section, we document the evolution of dynamic (wind, advection, turbulence) and
 329 thermodynamic (radiative cooling, moisture) parameters during the diurnal cycle. The aim is
 330 to analyze their relationships with LCC. It has been shown in SWA that moisture (Babic et al
 331 2019a) needed for saturation, and strong low level wind speed (Knippertz et al. 2011,
 332 Schuster et al. 2013) driving vertical mixing, are important factors for stratus formation. Do
 333 the core of those dynamic and thermodynamic parameters co-located with large LLCs also be
 334 observed in WCA ? We then investigate the atmospheric conditions driving low clouds by
 335 analyzing the evolution of wind speed and relative humidity (RH). The moisture flux
 336 (advection) and divergence are also investigated in this section. This is important to evaluate
 337 the behaviour (inflow or outflow) of moisture within the study area and the link with LCC
 338 formation and dissipation. Turbulence driven by nocturnal low-level jets has been proposed as
 339 an important factor for low cloud formation in SWA (Knippertz et al. 2011) through its
 340 contribution to vertical mixing. Therefore, we also analyze in this section the diurnal cycle of
 341 turbulent kinetic energy (TKE). All the computations are done from ground level (pressure <
 342 1000 hPa) to avoid influences of surface roughness.

343 4.1) Thermodynamic and dynamic conditions

344 We start the evaluation of atmospheric conditions relevant to low clouds by showing
 345 in **Fig 5** the JJAS average of three-hourly time-height sections of horizontal wind direction
 346 (vectors) and horizontal wind speed (contour) together with relative humidity (RH, shaded).
 347 Southwesterly flow up to 1200m (**Fig 5**) features the investigating area. Between 1200m and
 348 2000m, a minimum in wind speed (about 2m/s) corresponds to the veering from
 349 southwesterly to easterly. Above 2000m, easterlies reach 6m/s. Below 1000m, the maximum
 350 wind speed is observed between 22 LT and 04 LT (**Fig 5**). After 10LT, there is a decrease in
 351 RH simultaneously with a decrease in wind speed which starts to increase again in the
 352 evening (19 LT).

353 Three-hourly vertical profiles of cloud fraction averaged over 6°S-5°N/8°E-15°E are
 354 provided in **Fig 6**, along with vertical profiles of specific humidity, moisture advection,
 355 divergence of moisture advection, turbulent kinetic energy and static stability. The horizontal
 356 moisture advection is computed as follows : $Q_{adv} = qw$ where q is the specific humidity ($g.kg^{-1}$)
 357 and w is the sum of zonal (u) and meridional (v) wind components all are expressed
 358 in meters per second. The diurnal cycle of vertical profile of the low cloud cover (**Fig 6**) is in
 359 phase with **Fig 4** but differs in amount because low clouds are 3-D (**Fig 6**) and 2-D (**Fig 4**) as

360 mentioned in section 2.2. The maximum of low clouds is situated at about 800m of altitude at
 361 07 LT whereas the minimum in low clouds is observed at about 1500m of altitude at 19LT.
 362 The cloud deck height increases from 1000m at 10LT to reach 1500m at 16LT in response to
 363 an increase of the Atmospheric Boundary Layer (ABL) depth (not shown) due to entrainment
 364 and thermal expansion. Although the specific humidity stays rather constant, less than 16g/kg
 365 (**Fig 6b**) in the lower layers, low level moisture advection (**Fig 6c**) seems to play a substantial
 366 role in cloud occurrence. Positive (negative) advection denotes flow driven by southwesterly
 367 wind (easterly wind). Indeed, during the course of the night, advection supplies the area with
 368 moisture from the nearby Atlantic (Pokam et al. 2014), which enhances radiative cooling and
 369 cloud formation. This occurs despite the temporal mismatch between the height and time of
 370 occurrence of the largest cloud fraction and those of moisture advection. Maximum moisture
 371 advection observed between 22LT and 04LT - recorded at about 900m height - is associated
 372 with strong horizontal wind (**Fig 5**), whereas the largest cloud fraction is observed at about
 373 800m between 07LT and 10LT (**Fig 6a**). From the early afternoon to the evening, advection
 374 is weak due to reduced southwesterlies, and simultaneously, low clouds are partly dissipating.
 375 Above 1500m, easterly flow is the main driver of advection. In order to quantify the inflow or
 376 outflow moisture across our interested area, we calculate the divergence of the moisture

377 expressed by
$$\nabla Q_{adv} = \frac{dQ_{\alpha}}{dx} + \frac{dQ_{\beta}}{dy} \quad (1)$$
 where Q_{α} and Q_{β} are the zonal and
 378 meridional advectons, respectively. When computing moisture divergence with equation 1,
 379 negative (positive) values represent convergence (divergence). **Fig 6d** shows a strong
 380 moisture flux convergence in the low levels (< 600m) from 22LT to 04LT. Therefore, from
 381 the evening to late night, southwesterly (i.e. positive) inflow of moist air below 600m is prior
 382 to the occurrence of low clouds. Above 1500m, easterly flow acts to dry the upper layer
 383 (Kuete et al. 2019) since the air is drier over the Congo basin than over WCA at 700 hPa in
 384 JJAS (not shown). Moreover, moisture divergence is already present in layers between 700m
 385 and 900m (before the maximum advection) from 22LT and 07LT (**Fig 6d**). The diurnal cycles
 386 of the vertical profile of turbulent kinetic energy (TKE) and static stability are now analyzed.
 387 In West Africa (Knippertz et al. 2011, Schrage and Fink. 2012, Babic et al. 2019b) turbulent
 388 mixing driven by vertical wind shear plays an important role in stratus formation. At 19LT
 389 mixing at the surface is suppressed - as shown by low TKE value (< 0.1 m².s⁻²) (**Fig 6e**) - by
 390 strong static stability (**Fig 6f**). Note that positive (negative) values of static stability denote
 391 stable (unstable) atmosphere. Thereafter stability decreases during the night due to decrease in
 392 cooling (see section 4.3), leading to the moderate increase of TKE from 01LT to 04LT until

393 sunrise (07LT). This induces buoyancy of the moist air and vertical mixing in the lower layers
394 from the radiatively cooled surface (shown below) and contributes to LCCs formation during
395 late night. During daytime, especially in the early afternoon (13LT), TKE is the strongest (\sim
396 $0.8 \text{ m}^2\cdot\text{s}^{-2}$) leading to strong instability (**Fig 6e**). As a result, the cloud deck lifts
397 simultaneously with the LCC dissolution. Thus, depending on its intensity, turbulence
398 contributes to low cloud formation during the night and dissipation during the day along the
399 diurnal cycle in WCA.

400 The time-height evolution of RH in **Fig 5** shows large values $> 95\%$ below 1000m with a
401 maximum greater than 95% between 04LT and 07LT when low level winds are slowing
402 down. Near the surface, the moisture ratio is fairly close to saturation. Indeed, where RH is
403 greater than 80%, if such an air parcel is lifted, the pressure will decrease, and it will cool.
404 The time series of specific humidity (**Fig 6g**), RH (black line) and temperature (red line) (**Fig**
405 **6h**) at 790m (i.e 925hPa) where low clouds peak 07LT, are represented. Simultaneously with
406 the increase in RH from 94% to 98% between 01LT and 07LT, the specific humidity and
407 temperature respectively show a decrease of about 0.2g/kg and 0.5°C (the T° reaches its
408 minimum, about 19°C at 07LT). From 07LT, RH drops from 98% and reaches its minimum
409 of about 80% in the late afternoon, due to the diurnal warming since 07LT and T reaches its
410 maximum ($\sim 22^\circ\text{C}$) at 16LT. In the meantime, specific humidity continues to decrease to reach
411 its minimum (about 14g/kg) at 13LT. This suggests a moderate drying of the air mass over
412 WCA during daytime. This is accompanied by a significant reduction in cloud cover and an
413 increase in the cloud deck height (**Fig 6a**). Thereafter, RH starts to increase simultaneously
414 with the increase in specific humidity until 01LT while temperature has been decreasing since
415 16LT. After sunrise, wind speed drops (**Fig 6i**) due to strong turbulence (**Fig 6e**) compared to
416 nighttime where the atmosphere is stabilized (**Fig 6f**) by a cooled surface.

417 With the aim to investigate the degree of dependency between moisture advection
418 /divergence and LCCs fraction, scatter-plots are computed between 1) LCCs anomaly and
419 moisture advection at 925 hPa (i.e 790m above the ground) where the low clouds fraction
420 seems to peak, and 2) between LCCs anomaly and moisture flux divergence at 950 hPa (i.e
421 550m) where moisture convergence (**Fig 6d**) seems to be at its maximum. The LCCs anomaly
422 is computed following two steps: firstly, the spatial average considering only the most
423 overcasted pixels (cf **Fig 4a**) is performed to obtain LCCs hourly time series. Secondly, the
424 anomaly is computed by subtracting from each value of the time series the hourly mean of the

425 1952 values (122 days x 8 time slots x 2 years) of LCC time series. Results are presented
 426 respectively in **Fig 7** and **Fig 8**.

427 Correlation coefficient (CC) between LCC anomaly (referred to as “M”) and advection at 925
 428 hPa (**Fig 7**) increases from 0.31 at 19LT to 0.39 (maximum value) at 01LT simultaneously
 429 with an increase in advection (Adv) as shown in **Fig 6c**. At the same time, LCC anomaly
 430 switches from a negative value (M=-11%) at 19LT to a positive value at 01LT (M=2%). From
 431 01LT to 07LT, M is positive and is increasing to peak at 07LT (M=21%), fingerprinting an
 432 expansion in LCC. During daytime, M decreases from 3% at 10LT to reach its minimum of -
 433 13% at 16LT. At 950 hPa (**Fig 8**) there is strong moisture convergence along the diurnal cycle
 434 compared to 925 hPa (level of cloud maximum) where divergence has already taken place
 435 (**Fig 6d**) between 01LT and 07LT. Conversely, the largest LCC anomaly at 07LT is weaker at
 436 950 hPa (**Fig 8**) compared to 925 hPa (**Fig 7**). This suggests that near surface moisture is
 437 transported to the upper level to reach saturation.

438 4.2) Main contributors to moisture advection

439 We show in the previous section (**Fig 6c**) that advection supplies the area in moisture that is
 440 necessary for LCCs formation. The moisture advection is computed as $Q_{adv} = qw$. Then,
 441 the changes in moisture advection are the result of horizontal wind (w) and/or specific
 442 humidity (q) changes. This means that moisture advection increases (decreases) due to
 443 increases (decreases) in specific humidity and/or increases (decreases) in wind speed. In order
 444 to quantify whether q or w is the main contributor to moisture advection, the advection
 445 changes or tendencies are computed. In the following steps, we applied partial derivation to

$$446 \underbrace{Q_{adv}}_I \text{ with respect to time and the result is as follows: } \underbrace{q \frac{\partial w}{\partial t}}_{II} + \underbrace{w \frac{\partial q}{\partial t}}_{III} \quad (2)$$

447 where the term I is the moisture advection changes, the term II is the wind contribution and
 448 the term III is moisture contribution to total changes. To compute tendencies, we have applied
 449 the serial development of Taylor at any given time t_i . The results are shown in **Fig 9**. Note
 450 that at time t in **Fig 9**, one should understand the plot as the decrease or increase of moisture
 451 advection with respect to time t-1. For example, strong positive values at 19LT do not mean
 452 that moisture advection is stronger at 19LT than 07LT, but instead higher at 19LT with
 453 respect to 16 LT (the prior time step). We see that whatever the time-slot, changes in moisture
 454 advection are primarily due to horizontal wind advection. The contribution of specific

455 humidity remains close to zero throughout the diurnal cycle. Whether they are positive or
 456 negative, the three-hourly variations in advection change below 500m are quite small. This is
 457 probably due to weak wind speed (less than $5m.s^{-1}$) in the lower layer. In **Fig 10**,
 458 contributions of zonal and meridional flows to moisture advection are drawn. As the
 459 contribution of specific humidity is close to zero ($w \frac{\partial q}{\partial t} \approx 0$), equation 2 can be rewritten as

$$\underbrace{\frac{\partial Q_{adv}}{\partial t}}_I \approx q \underbrace{\frac{\partial u}{\partial t}}_{II} + q \underbrace{\frac{\partial v}{\partial t}}_{III} \quad (3)$$

460 follows : where term II and III are respectively the zonal
 461 and meridional contributions to advection changes. We observed that the second part of the
 462 night is characterized by a small decrease in zonal and meridional advection below 500m. The
 463 largest changes in advection (zonal and meridional) are observed below 1500m and switch
 464 from negative (advection decrease) in the morning to positive (advection increase) in the
 465 evening. During the course of the diurnal cycle, whether the variability is negative or positive,
 466 changes in advection are mainly related to zonal advection change.

467 **4.3 Relative humidity changes and cooling**

468 Here, we analyze the changes in relative humidity simultaneously with radiative
 469 cooling. Note that cooling rate is expressed as the temporal variation of potential temperature
 470 (θ). Changes in relative humidity (RH) are the result of changes in specific humidity (q) and
 471 temperature (T). In order to quantify which of q or T have the strongest contribution to RH
 472 changes and consequently to low level cloud formation, vertical profiles of their respective
 473 contribution are computed using ERA5 reanalysis. Assuming that relative humidity is
 474 expressed by $RH = e/e_s$ where e is water vapor pressure and e_s is the saturated water
 475 vapor pressure. Note that e_s is a function of temperature and is obtained according to Clausius

476 Clapeyron relation $\frac{\partial e_s}{\partial T} = \frac{L_v e_s}{R_v T^2}$ and water vapor pressure is expressed according to

477 $e = \frac{q}{0.378q + 0.622} P$. In these expressions, T is the air temperature (in kelvin), P is air
 478 pressure (in hPa), L_v is the latent heat of vaporization ($2.5.10^6 J.kg^{-1}$) and
 479 $R_v = 461.5 J.kg^{-1} K^{-1}$ is the gas constant of water vapor. Given the expression of RH, the
 480 contribution of T and q to RH changes is given (Babić et al. 2019a, Hannak et al. 2016) by
 481 equation

$$\underbrace{\frac{\partial RH}{\partial t}}_I = \underbrace{\frac{P}{e_s} \frac{0.622}{(0.378q + 0.622)^2} \frac{\partial q}{\partial t}}_{II} - \underbrace{\frac{P}{e_s} \frac{qL_v}{(0.378q + 0.622)R_v T^2} \frac{\partial T}{\partial t}}_{III} \quad (4)$$

482 where term
 483 I is the total RH changes, term II is q contribution and term III is T contribution. Because of
 484 the minus sign before term III, a positive (negative) value of that term signifies cooling
 485 (heating). The calculation of tendencies is performed only from late evening to early morning
 486 to emphasize cloud formation (i.e 19LT to 07LT). Results are presented in **Fig 11**. During the
 487 course of the night, there is an increase in RH but the rate of increase is quite different across
 488 the three-hourly timestep. In the early evening (at 19LT), there is a strong increase in RH
 489 below 500m with a maximum of about +7%/h, though the increasing tendency decreases with
 490 height. During the course of the night, the increasing rate of RH gradually decreases in the
 491 lower layer and reaches about +3%/h at 07LT. But the reverse is observed above 1500m
 492 where RH increases during the night. Above 1500m, the contribution of q to RH changes is
 493 more pronounced. On average (**Fig 11f**) and during almost all the night, cooling contributes
 494 100% to RH changes (**Fig 11f**) in the lower layer with an average cooling rate of about -
 495 0.6K/h (**Fig 11g**), even though small contribution of specific humidity (about 5%) is
 496 noticeable at 19LT below 500m. The observed nighttime evolution of cooling (**Fig 11g**)
 497 shows a strong cooling rate (about -1.3K/h) in the early evening probably due to rapid thermal
 498 inversion over land after sunset coinciding with the increase in moisture advection (**Fig 9 &**
 499 **Fig 10**). Note that the increase (decrease) of cooling rate expresses the increase (decrease) in
 500 cooling. This cooling gradually decreases during the course of the night and reaches -0.3K/h
 501 at 07LT when the low cloud cover is at its maximum (**Fig 6a**).

502 4.4) Surface energy and radiative balance

503 Because low clouds are mostly confined in the boundary layer, which is frequently
 504 thermodynamically connected to Earth's surface, our understanding of cloud formation also
 505 demands the understanding of surface processes. Energy release from the surface in response
 506 to solar radiation is the primary source of vertical motion or convective instability (Wood
 507 2012). Wood (2012) shows that the diurnal cycle of stratocumulus (Sc) clouds is strongly
 508 modulated by the diurnal cycle of solar radiation. The maximum of surface net shortwave
 509 radiation (**Fig 12a**, black line) reaches up to 450 W.m⁻² at 13LT with an interquartile range of
 510 about 77 W.m⁻². This is probably due to day-to-day variability of the transparency of the
 511 atmosphere. The surface net longwave radiation (R_L) is negative and shows much less
 512 variability. Note that net shortwave radiation (R_S) denotes the amount of solar radiation

513 minus the amount reflected (or albedo) by the earth's surface whereas R_L is the difference
 514 between the downward and upward thermal radiation at the earth's surface and net radiation
 515 (R^*) is the sum of R_L and R_S . At 13LT, R_S enhances the latent heat (**Fig 12b**, red line)
 516 which then leads to a large evaporation (**Fig 12c**). At this time, cloud fraction is decreasing
 517 and $R^* = 403 \text{ W.m}^{-2}$. At sunset (19LT), sensible heat becomes positive ($\sim +10.7 \text{ W.m}^{-2}$). It
 518 reaches a value of about $+3 \text{ W.m}^{-2}$ at 01LT. At the same time, R^* becomes negative and
 519 remains so during the night. It varies from -28 W.m^{-2} at 19LT to -26 W.m^{-2} at 01LT. Then, by
 520 contributing to the compensation of negative R^* (**Fig 12a**) from sunset to late night (01LT),
 521 downward sensible heat contributes to the development of a stable nocturnal surface layer and
 522 the enhancement of wind speed.

523 A conceptual model summarizing the processes of low cloud formation and dissipation
 524 along the diurnal cycle for WCA is proposed in **Fig 13**, showing evening (19, 22 LT), late
 525 night (01, 04, 07 LT) and daytime (10, 13, 16 LT) processes. In the evening, the horizontal
 526 advection of cool and moist air from the nearby Atlantic by the low level southwesterlies
 527 associated with strong moisture convergence of about $14 \text{ s}^{-1} \text{ g.kg}^{-1}$ leads to a strong radiative
 528 cooling of about -1.4 K/h below 500m which suppressed mixing. Consequently, there is no
 529 clouds formation. The horizontal wind speed is faster with a maximum value of about 4 m.s^{-1}
 530 simultaneously with the downward sensible heat which contributes to the stabilizing of the
 531 near surface layer.

532 During the late night, wind speed weakens. Then, moisture convergence also weakens as
 533 advection decreases, leading to decrease in cooling. As the cloud deck is formed, the cooling
 534 weakens at the surface (**Fig 11g**), and the TKE moderately increases up to $0.4 \text{ m}^2.\text{s}^{-2}$ favoring
 535 vertical mixing and maintaining the cloud deck. This is in agreement with the study by
 536 Schrage and Fink (2012), supporting that vertical transport of moisture contributes to cloud
 537 formation. After the cloud deck is formed, an increase of cooling at its top (i.e above 1000m,
 538 see **Fig 11g**) contributes to stabilizing as it is partly compensated by latent heating. Indeed,
 539 the level at which cloud fraction is maximum coincides with the level of strong moisture
 540 divergence (**Fig 6d**). Then, it seems like there is a competition between outflow of moisture
 541 and the turbulent vertical transport of moisture. We hypothesize that the altitude at which
 542 clouds form is first emptied partially of its moisture, leaving space for well mixed moisture
 543 from the lower layers which then condensates to form clouds.

544 During daytime, solar radiation heats the cloud top. Consequently, cooling at the top is
545 suppressed and cloud droplets evaporate. This reduces the cloud's thickness then leads to their
546 dissipation. Below the cloud deck, strong turbulence ($>0.4 \text{ m}^2\cdot\text{s}^{-2}$) which is accompanied by
547 the largest R^* ($\sim 403 \text{ W}\cdot\text{m}^{-2}$) acts also to destroy the clouds layer. At the same time, wind
548 speed is the weakest, the cloud layer rises and is less compact.

549 **5) Conclusion and discussion**

550 The aim of this study is to establish a picture of the dynamic and thermodynamic
551 processes under which LCCs grow in WCA across the diurnal cycle during the JJAS cloudy
552 main dry season. Our analysis is based mostly on ERA5 reanalysis. Before any use of ERA5
553 data, a short validation with satellite (Terra and Aqua MODIS) and ground-based
554 observations (EECRA) is made in order to show the capability of ERA5 to represent the
555 diurnal cycle and spatial distribution of LCCs. Three-hourly spatial evolution of LCCs from
556 ERA5 and EECRA in addition to LWP and TWV are drawn. We also explored the dynamic
557 and thermodynamic conditions by analysing RH, wind speed, temperature, and specific
558 humidity. In addition, horizontal advection, cooling, convergence and static stability are also
559 computed to strengthen our analysis. The main findings of our study are as follows:

560

561 1) Despite an underestimation of LCCs by ERA5, it captures well the mean spatial
562 distribution of low clouds as compared to EECRA and MODIS observations. The
563 LCCs diurnal cycles in EECRA and ERA5 are also well correlated although ERA5
564 struggles to produce enough clouds during the afternoon. The spatial evolution during
565 the diurnal cycle shows that LCCs fraction is the weakest at 19LT. Then, it starts to
566 grow at 22LT from south-Cameroon. LCCs fraction peaks during late night (04-07
567 LT) over windward slopes and coastal plains. After sunrise at 07LT, LCCs display a
568 north-south gradient (more LCCs over Gabon than Cameroon) which vanishes as
569 LCCs cover diminishes overall till 19LT. Accordingly, the cloud liquid water content
570 shows similar evolution along the diurnal cycle.

571 2) WCA is subject in JJAS to a southwesterly flow in the low layers, a flow whose
572 intensity increases from the evening to 01 LT and advects humidity from the ocean to
573 the region. As shown in **Fig 5**, the large humidity content in the low layers in late
574 night is necessary for condensation and LCCs formation. There is strong moisture
575 convergence in the lower layer ($<500\text{m}$) while strong moisture advection is recorded
576 from 19LT to 01LT at 900m of altitude.

- 577 3) We calculated the contributions of specific humidity and also zonal and meridional
578 wind to humidity advection. During the diurnal cycle, advection changes are mostly
579 due to change in horizontal wind, with zonal wind acting as the main driver of these
580 changes as compared to meridional wind. The contribution of specific humidity is
581 quasi close to zero and does not contribute to advection changes.
- 582 4) We have also investigated the contributions of temperature and specific humidity to
583 RH changes from the evening to early morning, i.e during clouds formation. The first
584 insight shows that temperature contributes nearly 100% to RH changes. From 19LT,
585 the strong radiative cooling at the surface increases relative humidity by about 8%
586 near the surface. During the course of the night, RH gradually increases. Conversely,
587 while below 1000m the rate of RH changes is decreasing, the contrary is observed
588 above 1000m. Changes in RH are mostly due to variations in cooling.
- 589 5) While horizontal advection of moisture is shown to be a precondition to LCCs
590 formation, another process is necessary for cloud formation. Vertical upward mixing
591 of moisture from the lower layer during nighttime due to moderate TKE is necessary
592 for cloud formation. This vertical mixing is important for saturation. Once the cloud
593 deck is formed in stable condition, cooling weakens at the surface, strong cooling at
594 the top of the cloud deck is partially compensated by latent heat. All these processes
595 help to maintain the cloud deck. During daytime, low clouds dissipate in response to
596 strong thermodynamic instability due to the increase of solar radiation.
- 597 6) Finally, we can conclude that, the LCCs in WCA are formed owing to the combination
598 of the horizontal advection of cooler air, turbulent vertical mixing of moisture.
599 Radiative cooling at the top helps to maintain the cloud deck once it has formed. The
600 dissipation of LCCs is mainly due to strong turbulence.

601
602 The use of ERA5 may lead to slight discrepancies when calculating some quantities. For
603 instance, the calculation of relative humidity tendencies directly using RH from ERA5 may
604 lead to small discrepancies if we compute RH tendencies as the sum of term II and term III of
605 equation 4. Therefore, total RH tendencies or changes in this study is the sum of term II and
606 term III of equation 4 rather than the RH variable itself. We account for these differences to
607 the complexity of the ERA5 data assimilation schemes. In addition to using only two years of
608 data, another bias using ERA5 is the overestimation of low cloud over south Cameroon
609 compared to what is found in Dommo et al. (2018) (see their figure 2d). This is because
610 ERA5 does not yet make any difference between stratiform and cumuliform clouds. Low

611 clouds in south Cameroon may be mainly dominated by cumuliform clouds particularly
612 cumulonimbus. Therefore, in situ measurements and radio soundings are needed to
613 disentangle and quantify precisely the phenomena which drive observed LCCs formation,
614 maintenance and dissipation over WCA. Nevertheless, the use of ERA5 allows us to analyse a
615 panel of atmospheric processes relevant to LCCs in WCA. Results show some similar
616 findings to southern west Africa (SWA): for instance, horizontal cold air advection after
617 sunset and radiative cooling (Babic et al. 2019, Lehou et al. 2020) also drive the strong
618 decrease in nighttime temperatures. Additionally, low level convergence (Kniffka et al 2019)
619 is similar between SWA and WCA. Also demonstrated in this study is the role of upward
620 mixing of moisture that accumulates in the low layers. This result has also been highlighted
621 by Schrage and Fink (2012) in SWA. The added value of this work compared to what is found
622 in SWA is the range of TKE. Indeed, if TKE is greater than $0.4 \text{ m}^2 \cdot \text{s}^{-2}$ in WCA, it acts to
623 destroy the cloud layer.

624
625 The datasets used in this study are completely different from those used in similar studies over
626 SWA where studies are mostly based on in situ observations and radiosondes. They were able
627 to distinguish different phases in LCCs evolution along the diurnal cycle (Babic et al. 2019,
628 Lehou et al. 2020, Alder et al. 2019), the atmospheric processes relevant to each phase, and to
629 quantify them precisely. For instance, Alder et al. (2019) show that horizontal cold air
630 advection contributes to 50% of cooling, whereas radiative flux divergence and sensible heat
631 flux divergence contribute 20% and 22% (respectively) to cooling. Additionally, they
632 highlighted the intensification of low-level jets during the jet phase. These are processes
633 which we could not explore for WCA, due to the lack of observational datasets. Besides,
634 Knippertz et al. (2011) also show the effects of aerosols on LCCs formation whereas Deetz et
635 al. (2018) show that transitions from stratus to cumulus are highly sensitive to aerosols. On
636 the other hand, the effects of gravity waves are not yet explored in WCA as it is pointed out
637 by Babic et al. (2019b) for SWA. Therefore, many questions remain unanswered concerning
638 the processes relevant to LCCs in WCA. For instance, in SWA, a clear characteristic between
639 cloudy and non-cloudy nights is made, followed by the main factors leading to these
640 differences. Nevertheless, this study has allowed us to lay the groundwork for an in-depth
641 study of low clouds in WCA, a region that is still very poorly documented. This study also
642 allowed us to considerably improve our knowledge of the LCCs for the region compared to
643 the work of Dommo et al. (2018) and can help us to ameliorate our understanding of the
644 climatic characteristics of the region and the improvement of the regional climate model

645 simulations.

References

- 646
647 Ackerman SA, Strabala KI, Menzel WP, Frey R, Moeller C, Gumley L (1998)
648 Discriminating clear sky from clouds with MODIS. *J Geophys Res: Atmospheres*
649 103:32141–32157. doi: 10.1029/1998jd200032
- 650 Adler B, Babić K, Kalthoff N, Lohou F, Lothon M, Dione C, Pedruzo-Bagazgoitia X,
651 Andersen H (2019) Nocturnal low-level clouds in the atmospheric boundary layer
652 over southern West Africa: an observation-based analysis of conditions and
653 processes. *Atmos Chem Phys* 19:663–681. doi: 10.5194/acp-19-663-2019
- 654 Babić K, Kalthoff N, Adler B, Quinting JF, Lohou F, Dione C, Lothon M (2019b) What
655 controls the formation of nocturnal low-level stratus clouds over southern West Africa
656 during the monsoon season? *Atmos Chem Phys* 19:13489–13506. doi: 10.5194/acp-
657 19-13489-2019
- 658 Babić K, Adler B, Kalthoff N, Andersen H, Dione C, Lohou F, Lothon M, Pedruzo-
659 Bagazgoitia X (2019a) The observed diurnal cycle of low-level stratus clouds over
660 southern West Africa: a case study. *Atmos Chem Phys* 19:1281–1299. doi:
661 10.5194/acp-19-1281-2019
- 662 Cermak J (2012) Low clouds and fog along the South-Western African coast — Satellite-
663 based retrieval and spatial patterns. *Atmos Res* 116:15–21. doi:
664 10.1016/j.atmosres.2011.02.012
- 665 Chen T, Rossow WB, Zhang Y (2000) Radiative Effects of Cloud-Type Variations. *J Clim*
666 13:264–286. doi: 10.1175/1520-0442(2000)013<0264:reoctv>2.0.co;2
- 667 Danso DK, Anquetin S, Diedhiou A, Lavaysse C, Koba A, Touré NE (2019) Spatio-
668 temporal variability of cloud cover types in West Africa with satellite-based and
669 reanalysis data. *Q J R Meteorol Soc* 145:3715–3731. doi: 10.1002/qj.3651

- 670 Deetz K, Vogel H, Knippertz P, et al (2018) Numerical simulations of aerosol radiative
671 effects and their impact on clouds and atmospheric dynamics over southern West
672 Africa. *Atmos Chem Phys* 18:9767–9788. doi: 10.5194/acp-18-9767-2018
- 673 Dommo A, Philippon N, Vondou DA, Sèze G, Eastman R (2018) The June–September Low
674 Cloud Cover in Western Central Africa: Mean Spatial Distribution and Diurnal
675 Evolution, and Associated Atmospheric Dynamics. *J Clim* 31:9585–9603. doi:
676 10.1175/jcli-d-17-0082.1
- 677 Fotso-Nguemo TC, Vondou DA, Tchawoua C, Haensler A (2016) Assessment of simulated
678 rainfall and temperature from the regional climate model REMO and future changes
679 over Central Africa. *Clim Dyn* 48:3685–3705. doi: 10.1007/s00382-016-3294-1
- 680 Fotso-Nguemo TC, Vondou DA, Pokam WM, Yepdo Djomou Z, Diallo I, Haensler A,
681 Djiotang Tchotchou LA, Kamsu-Tamo PH, Gaye AT, Tchawoua C (2017) On the
682 added value of the regional climate model REMO in the assessment of climate change
683 signal over Central Africa. *Clim Dyn* 49:3813–3838. doi: 10.1007/s00382-017-3547-7
- 684 Garratt JR (1999) *The atmospheric boundary layer*. Cambridge University Press
- 685 Hahn CJ, Warren SG, London J (1995) The Effect of Moonlight on Observation of Cloud
686 Cover at Night, and Application to Cloud Climatology. *J Clim* 8:1429–1446. doi:
687 10.1175/1520-0442(1995)008<1429:teomoo>2.0.co;2
- 688 Hahn C, Warren S (2007) A Gridded Climatology of Clouds over Land (1971–96) and Ocean
689 (1954–97) from Surface Observations Worldwide. Carbon Dioxide Information
690 Analysis Center (CDIAC) Datasets. doi: 10.3334/cdiac/cli.ndp026e
- 691 Hannak L, Knippertz P, Fink AH, et al (2017) Why Do Global Climate Models Struggle to
692 Represent Low-Level Clouds in the West African Summer Monsoon? *J Clim*
693 30:1665–1687. doi: 10.1175/jcli-d-16-0451.1

- 694 Hartmann DL, Ockert-Bell ME, Michelsen ML (1992) The Effect of Cloud Type on Earth's
695 Energy Balance: Global Analysis. *J Clim* 5:1281–1304. doi: 10.1175/1520-
696 0442(1992)005<1281:teocto>2.0.co;2
- 697 Hersbach H, Rosnay Pde, Bell B (2018) Operational global reanalysis progress, future
698 directions and synergies with NWP. *European Centre for Medium Range Weather*
699 *Forecasts*
- 700 Klein SA, Hartmann DL (1993) The Seasonal Cycle of Low Stratiform Clouds. *J Clim*
701 6:1587–1606. doi: 10.1175/1520-0442(1993)006<1587:tscols>2.0.co;2
- 702 Kniffka A, Knippertz P, Fink AH (2019) The role of low-level clouds in the West African
703 monsoon system. *Atmos Chem Phys* 19:1623–1647. doi: 10.5194/acp-19-1623-2019
- 704 Knippertz P, Fink AH, Schuster R, Trentmann J, Schrage JM, Yorke C (2011) Ultra-low
705 clouds over the southern West African monsoon region. *Geophys Res Lett*. doi:
706 10.1029/2011gl049278
- 707 Kuete G, Mba WP, Washington R (2019) African Easterly Jet South: control, maintenance
708 mechanisms and link with Southern subtropical waves. *Clim Dyn* 54:1539–1552. doi:
709 10.1007/s00382-019-05072-w
- 710 Lei Y, Letu H, Shang H, Shi J (2020) Cloud cover over the Tibetan Plateau and eastern
711 China: a comparison of ERA5 and ERA-Interim with satellite observations. *Clim Dyn*
712 54:2941–2957. doi: 10.1007/s00382-020-05149-x
- 713 Lohou F, Kalthoff N, Adler B, Babi K, Dione C, Lothon M, Pedruzo-Bagazgoitia X,
714 Zouzoua M (2020) Conceptual model of diurnal cycle of low-level stratiform clouds
715 over southern West Africa. *Atmos Chem Phys* 20:2263–2275. doi: 10.5194/acp-20-
716 2263-2020

- 717 Maddux BC, Ackerman SA, Platnick S (2010) Viewing Geometry Dependencies in MODIS
718 Cloud Products. *J Atmos Oceanic Technol* 27:1519–1528. doi:
719 10.1175/2010jtecha1432.1
- 720 Mba WP, Longandjo G-NT, Moufouma-Okia W, Bell JP, James R, Vondou DA, Haensler
721 A, Fotso Nguemo TC, Guenang GM, Djiotang Tchotchou AL, Kamsu-Tamo PH,
722 Takong RR, Grigory N, Lennard CJ, Dosio A (2018) Consequences of 1.5 °C and 2 °C
723 global warming levels for temperature and precipitation changes over Central Africa.
724 *Environ Res Lett* 13:055011. doi: 10.1088/1748-9326/aab048
- 725 Oreopoulos L (2005) The impact of subsampling on MODIS level-3 statistics of cloud
726 optical thickness and effective radius. *IEEE Transactions on Geoscience and Remote*
727 *Sensing* 43:366–373. doi: 10.1109/tgrs.2004.841247
- 728 Paluch IR, Lenschow DH (1991) Stratiform Cloud Formation in the Marine Boundary
729 Layer. *J Atmos Sci* 48:2141–2158. doi: 10.1175/1520-
730 0469(1991)048<2141:scfitm>2.0.co;2
- 731 Philippon N, Cornu G, Monteil L, Gond V, Moron V, Pergaud J, Sèze G, Bigot S, Camberlin
732 P, Doumenge C, Fayolle A, Ngomanda A (2019) The light-deficient climates of
733 western Central African evergreen forests. *Environ Res Lett* 14:034007. doi:
734 10.1088/1748-9326/aaf5d8
- 735 Pilié RJ, Mack EJ, Rogers CW, Katz U, Kocmond WC (1979) The Formation of Marine Fog
736 and the Development of Fog-Stratus Systems along the California Coast. *J Appl*
737 *Meteorol* 18:1275–1286. doi: 10.1175/1520-0450(1979)018<1275:tfomfa>2.0.co;2
- 738 Pokam WM, Bain CL, Chadwick RS, Graham R, Sonwa DJ, Mkankam Kamga F (2014)
739 Identification of Processes Driving Low-Level Westerlies in West Equatorial Africa. *J*
740 *Clim* 27:4245–4262. doi: 10.1175/jcli-d-13-00490.1

- 741 Schrage JM, Augustyn S, Fink AH (2007) Nocturnal stratiform cloudiness during the West
742 Africa monsoon. *Meteorol Atmos Phys* 96: 73-86. doi: 10.1007/s00703-006-0194-7
- 743 Schrage JM, Fink AH (2012) Nocturnal Continental Low-Level Stratus over Tropical West
744 Africa: Observations and Possible Mechanisms Controlling Its Onset. *Mon Weather*
745 *Rev* 140:1794–1809. doi: 10.1175/mwr-d-11-00172.1
- 746 Schuster R, Fink AH, Knippertz P (2013) Formation and Maintenance of Nocturnal Low-
747 Level Stratus over the Southern West African Monsoon Region during AMMA 2006.
748 *J Atmos Sci* 70:2337–2355. doi: 10.1175/jas-d-12-0241.1
- 749 Solomon S (2007) *Climate change 2007: the physical science basis*. Published for the IPCC
750 by Cambridge University Press
- 751 Sonkoué D, Monkam D, Fotso-Nguemo TC, Yepdo ZD, Vondou DA (2018) Evaluation and
752 projected changes in daily rainfall characteristics over Central Africa based on a multi-
753 model ensemble mean of CMIP5 simulations. *Theor Appl Climatol* 137:2167–2186.
754 doi: 10.1007/s00704-018-2729-5
- 755 Stephens GL (1978) Radiation Profiles in Extended Water Clouds. I: Theory. *J Atmos Sc*
756 35:2111–2122. doi: 10.1175/1520-0469(1978)035<2111:rpiewc>2.0.co;2
- 757 Stephens GL, Greenwald TJ (1991) The Earth's radiation budget and its relation to
758 atmospheric hydrology: 2. Observations of cloud effects. *J Geophys Res* 96:15325.
759 doi: 10.1029/91jd00972
- 760 Stevens B (2002) Entrainment in stratocumulus-topped mixed layers. *Q J R Meteorol Soc*
761 128:2663–2690. doi: 10.1256/qj.01.202
- 762 Sun J, Angal A, Xiong X, et al (2012) MODIS reflective solar bands calibration
763 improvements in Collection 6. *Earth Observing Missions and Sensors: Development,*
764 *Implementation, and Characterization II*. doi: 10.1117/12.979733

- 765 Tamoffo AT, Vondou DA, Pokam WM, Haenler A, Yepdo ZD, Fotso-Nguemo TC, Djiotang
766 Tchotchou LA, Nouayou R (2019a) Daily characteristics of Central African rainfall in
767 the REMO model. *Theor Appl Climatol* 137:2351–2368. doi: 10.1007/s00704-018-
768 2745-5
- 769 Tamoffo AT, Nikulin G, Vondou DA, Dosio A, Nouayou R, Wu M, Igri PM (2021) Process-
770 based assessment of the impact of reduced turbulent mixing on Congo Basin
771 precipitation in the RCA4 Regional Climate Model. *Clim Dyn*. doi: 10.1007/s00382-
772 020-05571-1
- 773 Vondou DA, Haensler A (2017) Evaluation of simulations with the regional climate model
774 REMO over Central Africa and the effect of increased spatial resolution. *Int J*
775 *Climatol* 37:741–760. doi: 10.1002/joc.5035
- 776 Wood R (2012) Stratocumulus Clouds. *Mon Weather Rev* 140:2373–2423. doi:
777 10.1175/mwr-d-11-00121.1
- 778 Zouzoua M, Lohou F, Assamoi P, Lothon M, Yoboue V, Dione C, Kalthoff N, Alder B,
779 Babic K, Pedruzo-Bagazgoitia X, Derrien S (2021) Breakup of nocturnal low-level
780 stratiform clouds during the southern West African monsoon season. *Atmos Chem*
781 *Phys* 21:2027–2051. doi: 10.5194/acp-21-2027-2021

782 **List of figures**

- 783 **1** Topography of the study area. Red triangles indicate the 18 EECRA stations used in this
784 study
- 785 **2** Diurnal cycle of low cloud fraction for each year from 1979 to 2019 (grey lines) and in
786 2014 (red line) and 2015 (black line) spatially averaged over 6°S-5°N/8°E-15°E. Land-
787 only pixels are considered
- 788 **3** Mean JJAS spatial distribution of low clouds cover in WCA from a) MODIS satellite
789 observation, b) ERA5 reanalysis, c) land station observation (EECRA) and d) diurnal
790 cycle of LCC. Triangles in panel c indicate EECRA stations. For diurnal cycle (d),
791 only ERA5 pixels documenting the 18 EECRA stations are used, and the error bars
792 indicate the standard deviation of diurnal cycle across the grid points corresponding to
793 EECRA stations. For EECRA observations, only stations recording at least 25% of the
794 data for the JJAS seasons over the 39-year EECRA observation have been used. The
795 diurnal cycle is computed within the green box considering only ERA5 pixels
796 documenting EECRA stations (**Fig 1**). The red dashed curve indicates the difference
797 between EECRA and ERA5
- 798 **4** Mean spatial evolution of low clouds cover during the diurnal cycle for ERA5 (panel a), and
799 EECRA (panel b). Black dots on panel a) are pixels with at least 80% of low cloud
800 fraction at 07LT. Triangles (panel b) indicates EECRA stations. For EECRA, only
801 stations (18) recording at least 25% of the data for the JJAS seasons over the 39-year
802 EECRA observation period have been used. Time series (panel c) of total column water
803 vapor (TWV, blue line) and total column cloud liquid water content (LWP, red line)
804 within the green box. Only ERA5 pixels the closest to EECRA stations (**Fig 1**) are
805 considered for times series computation.

806 **5** Time-height evolution of ERA5 relative humidity (shadings in %) and horizontal wind
807 speed in m/s (contour) averaged over 6°S-5°N/8°E-15°E. Only land pixels with at least
808 80% of low clouds cover at 07LT are considered for spatial average. The wind speed
809 values are indicated in red. The arrows show the horizontal wind vectors displayed as
810 usual on a lon-lat map. Computations are made from ground level (pressure < 1000
811 hPa)

812 **6** ERA5 Three-hourly vertical profiles from ground level of (a) cloud fraction (%), (b)
813 specific humidity, (c) moisture advection, (d) divergence of moisture advection, (e)
814 turbulent kinetic energy, and (f) static stability. Time series of g) specific humidity, h)
815 relative humidity (black line) and temperature (red line) and, i) horizontal wind speed at
816 925 hPa i.e about 790m from ground level. Spatial averages are made considering land-
817 only pixels which record at least 80% of low cloud at 07LT

818 **7** Scatter plots between low level cloud fraction anomaly and moisture advection at 925 hPa
819 during the diurnal cycle. The scatter plot is obtained by averaging land only pixels
820 which record at least 80% in low cloud fraction at 07LT within the box 6°S-5°N/8°E-
821 15°E for the period 2014-2015. For each time slot (01,04,07,10,13,16, 19 & 22LT), the
822 mean advection (Adv) and the mean low cloud cover anomaly (M) and correlation
823 coefficient (CC) are computed. The regression line between the two variables is
824 represented in black, and the reference line ($y=0$) is in green

825 **8** Same as fig 7 but between low cloud fraction anomaly and moisture divergence at 950 hPa.
826 For each time slot, Div denotes the mean divergence. Negative (positive) values of
827 divergence expressed moisture inflow (outflow)

828 **9** ERA5 Three-hourly vertical profiles of wind (blue line) and specific humidity (green line)
829 mean contribution to total advection change (red) from the ground level (pressure
830 <1000) averaged over 6°S-5°N/8°E-15°E for the period 2014-2015. Only land pixels

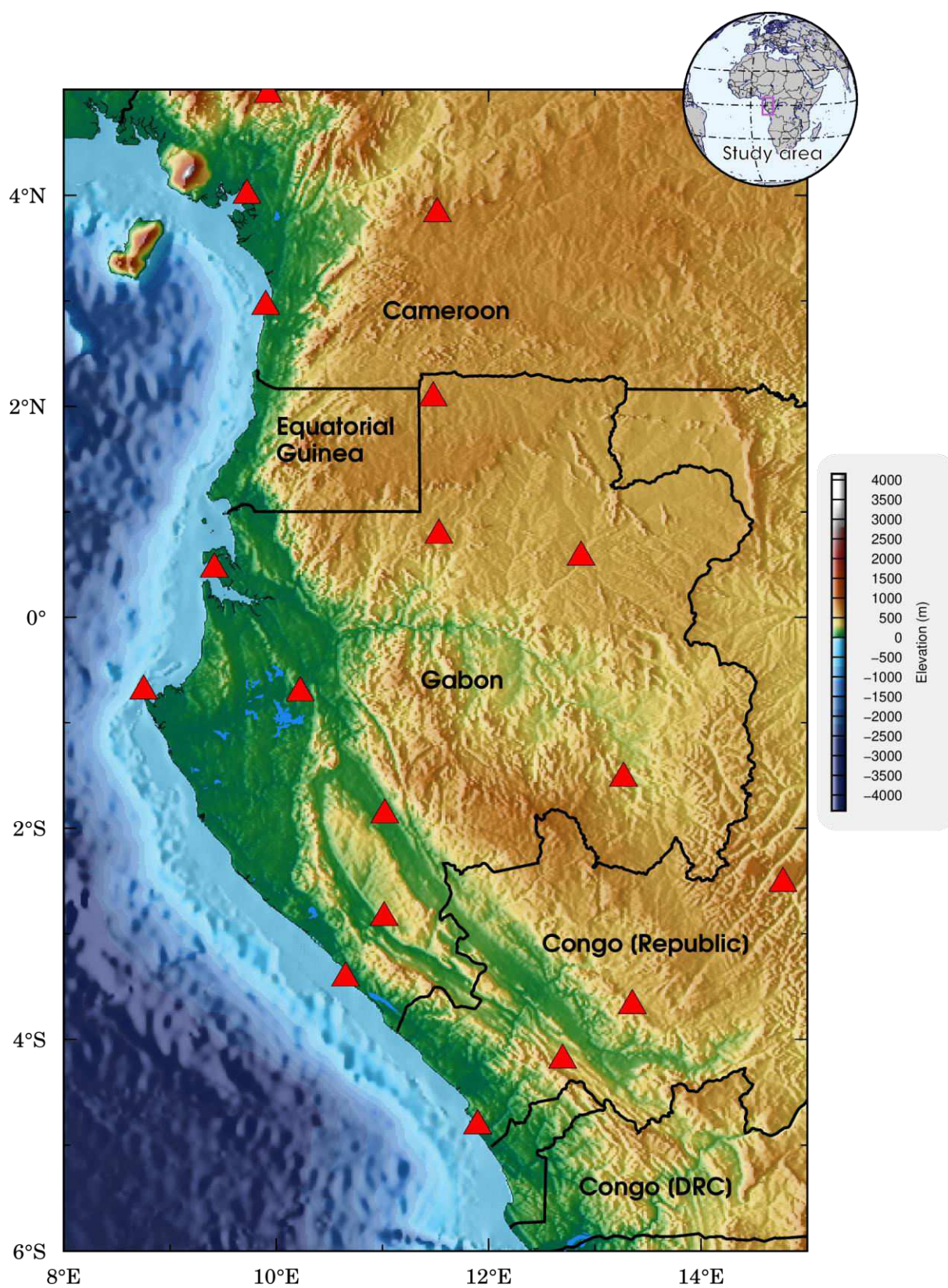
831 with at least 80% of cloud fraction at 07LT are considered for spatial average

832 **10** ERA5 Three-hourly vertical profiles of zonal (magenta) and meridional (cyan) wind
833 contribution to total advection change (black) from the ground level (pressure <1000)
834 within 6°S-5°N/8°E-15°E for the period 2014-2015. Only land pixels with at least 80%
835 of low cloud fraction at 07LT are considered for spatial average

836 **11** a-e) ERA5 vertical profiles of specific humidity (q) and temperature (T) contribution to
837 relative humidity (RH) changes from early evening to early morning (19, 22, 01, 04,
838 and 07LT). f) average for the five time slots. g) cooling rate from early evening to early
839 morning (19, 22, 01, 04, and 07LT). The magenta line is the average of the 5 time-slots.
840 Calculations are made from ground level (pressure < 1000hPa) considering land only
841 pixels with at least 80% of low cloud fraction at 07LT within 6°S-5°N/8°E-15°E for the
842 period 2014-2015

843 **12** Diurnal cycle of a) radiative balance (Net radiation: R^* , surface net shortwave radiation:
844 R_S , Net long wave radiation: R_L , b) energy balance (sensible heat, latent heat) and c)
845 evaporation within 6°S-5°N/8°E-15°E for the period 2014-2015. Only land pixels
846 recording at least 80% in low cloud fraction are considered for spatial average. Error
847 bars indicate the interquartile ranges

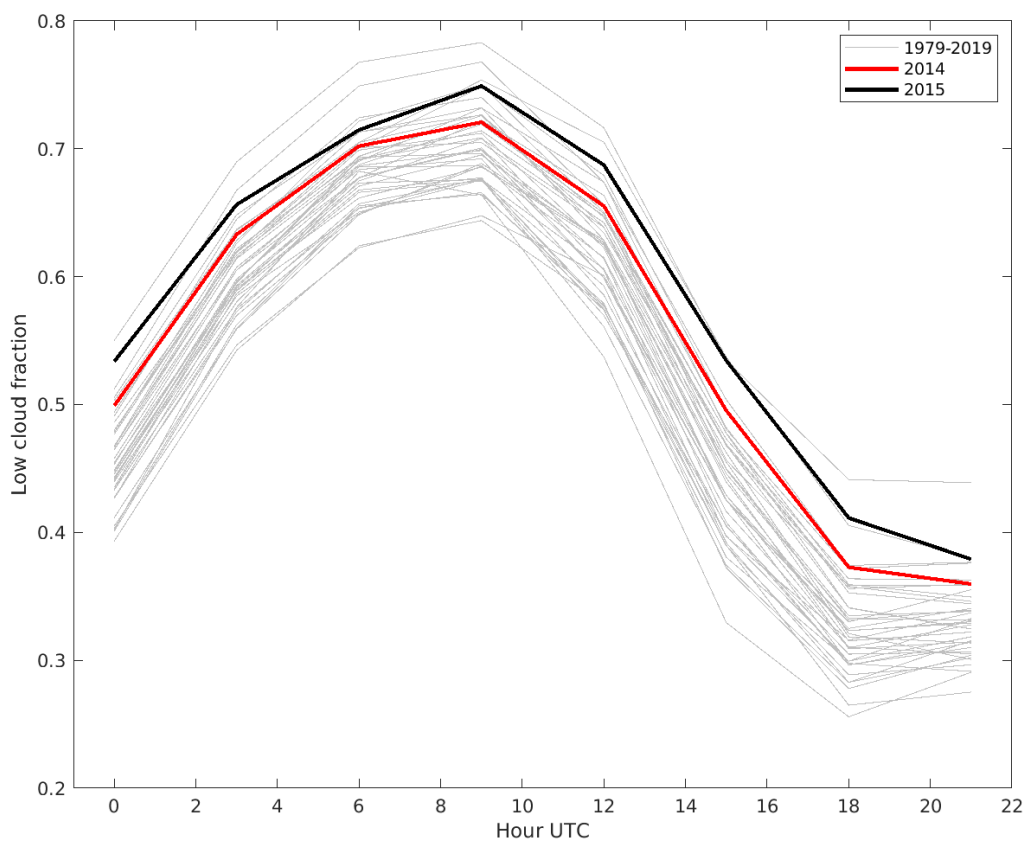
848 **13** Conceptual schematic model illustrating the cloud formation and dissipation processes
849 over WCA along the diurnal cycle. The dark blue lines represent the vertical profiles of
850 the horizontal wind with an indication of its maximum value at evening (19, 22 LT),
851 late night (01, 04, 07 LT) and daytime (10, 13, 16 LT). The dark curled arrows
852 symbolize mixing due to nocturnal turbulence. Maximum values for the contribution of
853 each process are given. Each value is obtained from ERA5 within 6°S-5°N/8°E-15°E
854 for the period 2014-2015



855

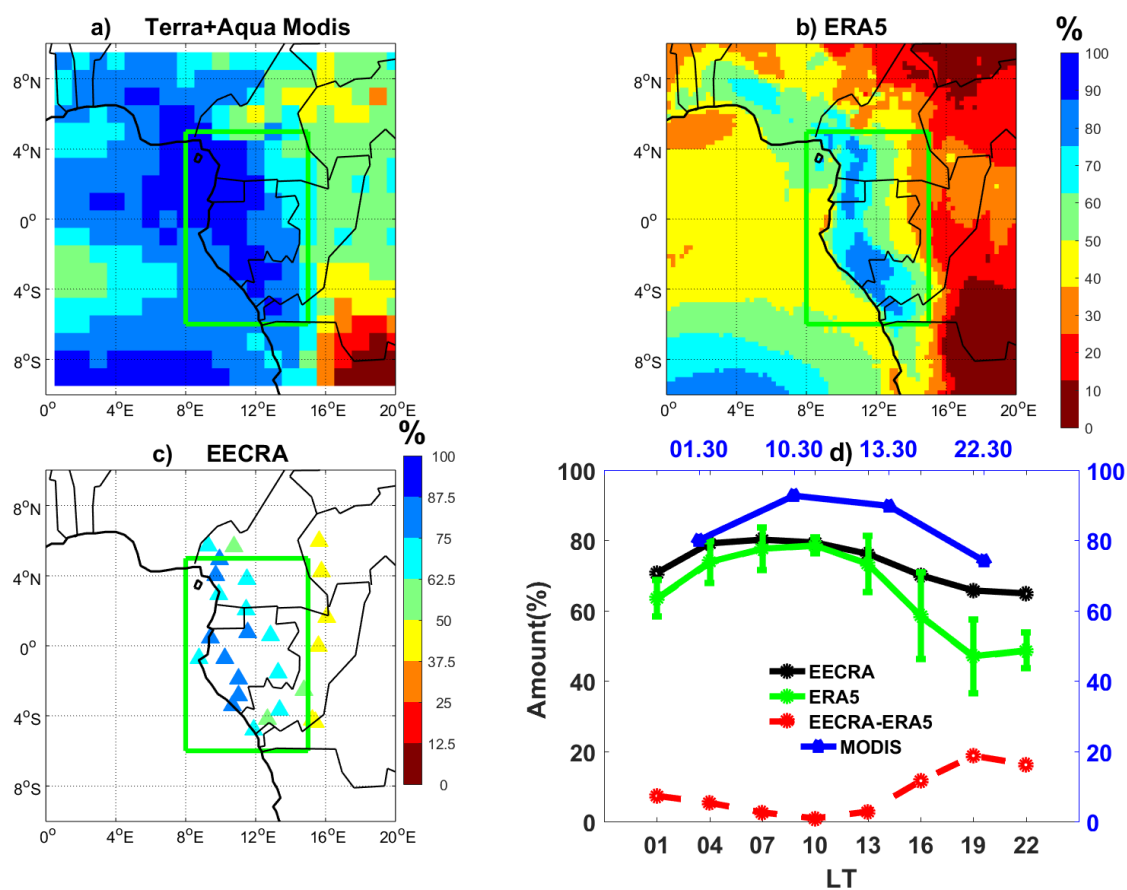
856 **Fig. 1** Topography of the study area. Red triangles indicate the 18 EECRA stations used in

857 this study



858

859 **Fig. 2** Diurnal cycle of low cloud fraction for each year from 1979 to 2019 (grey lines) and in
860 2014 (red line) and 2015 (black line) spatially averaged over 6°S-5°N/8°E-15°E. Land-
861 only pixels are considered



862

863 **Fig. 3** Mean JJAS spatial distribution of low clouds cover in WCA from a) MODIS satellite

864 observation, b) ERA5 reanalysis, c) land station observation (EECRA) and d) diurnal

865 cycle of LCC. Triangles in panel c indicate EECRA stations. For diurnal cycle (d),

866 only ERA5 pixels documenting the 18 EECRA stations are used, and the error bars

867 indicate the standard deviation of diurnal cycle across the grid points corresponding to

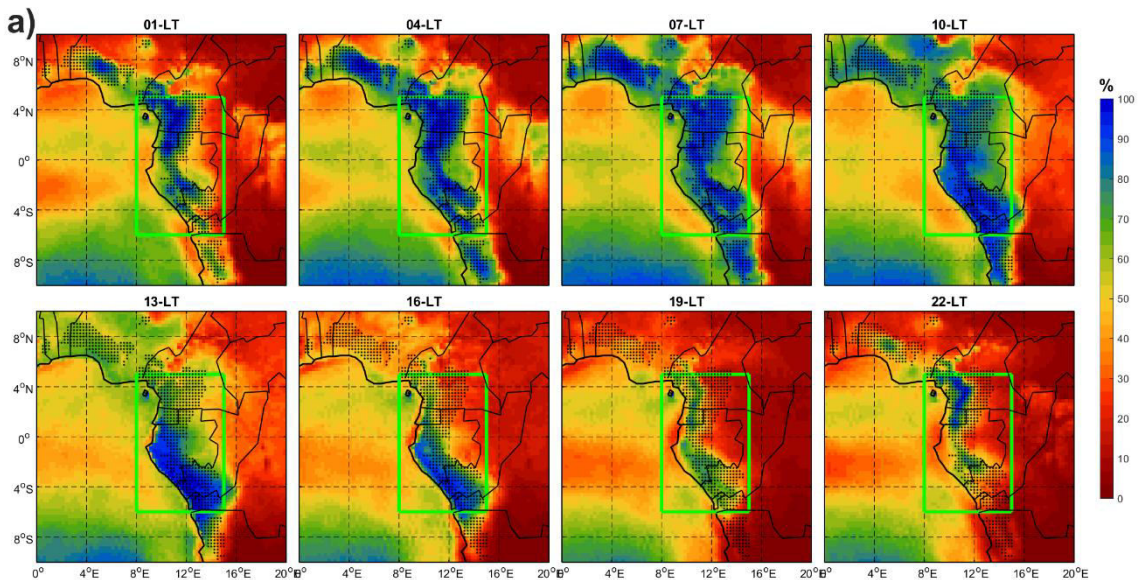
868 EECRA stations. For EECRA observations, only stations recording at least 25% of the

869 data for the JJAS seasons over the 39-year EECRA observation have been used. The

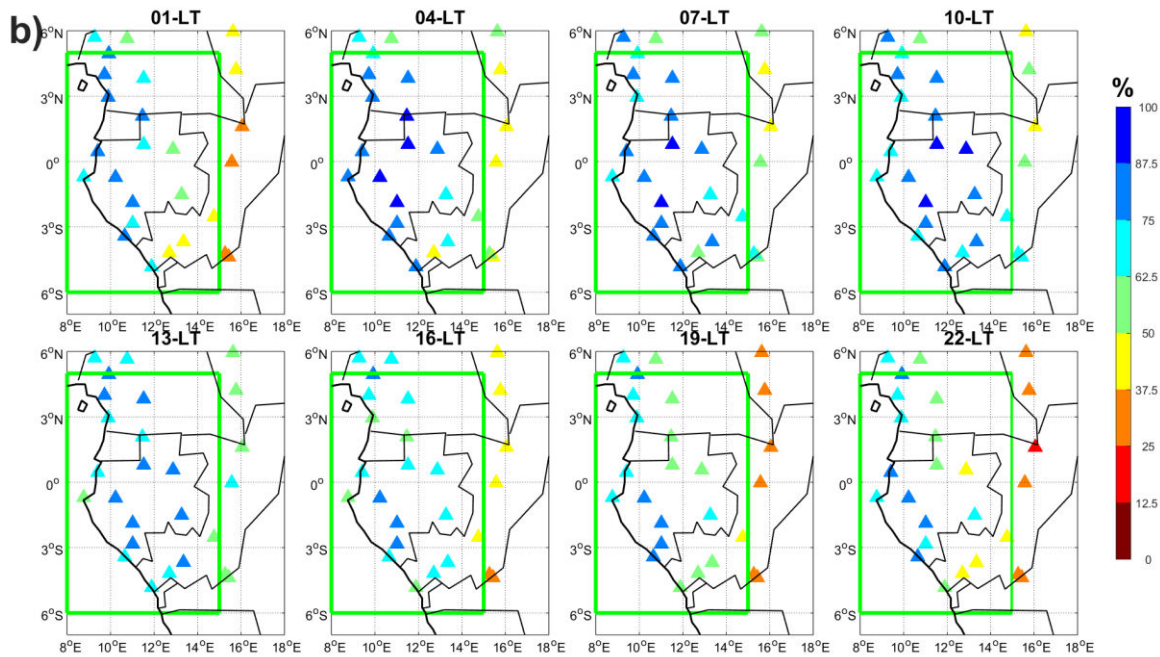
870 diurnal cycle is computed within the green box considering only ERA5 pixels

871 documenting EECRA stations (**Fig 1**). The red dashed curve indicates the difference

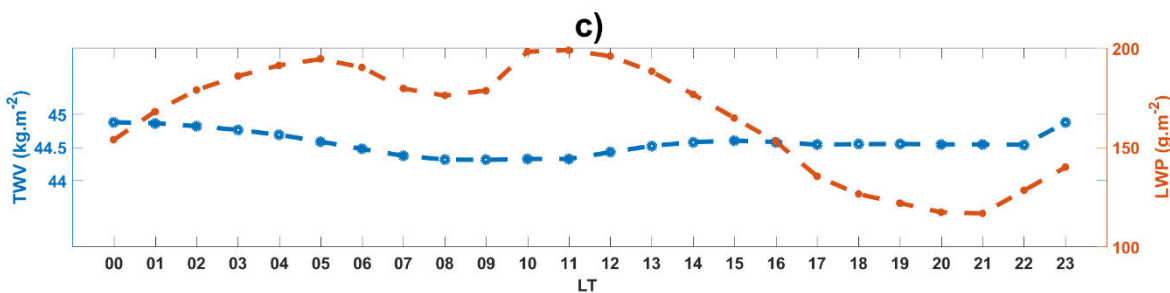
872 between EECRA and ERA5



873



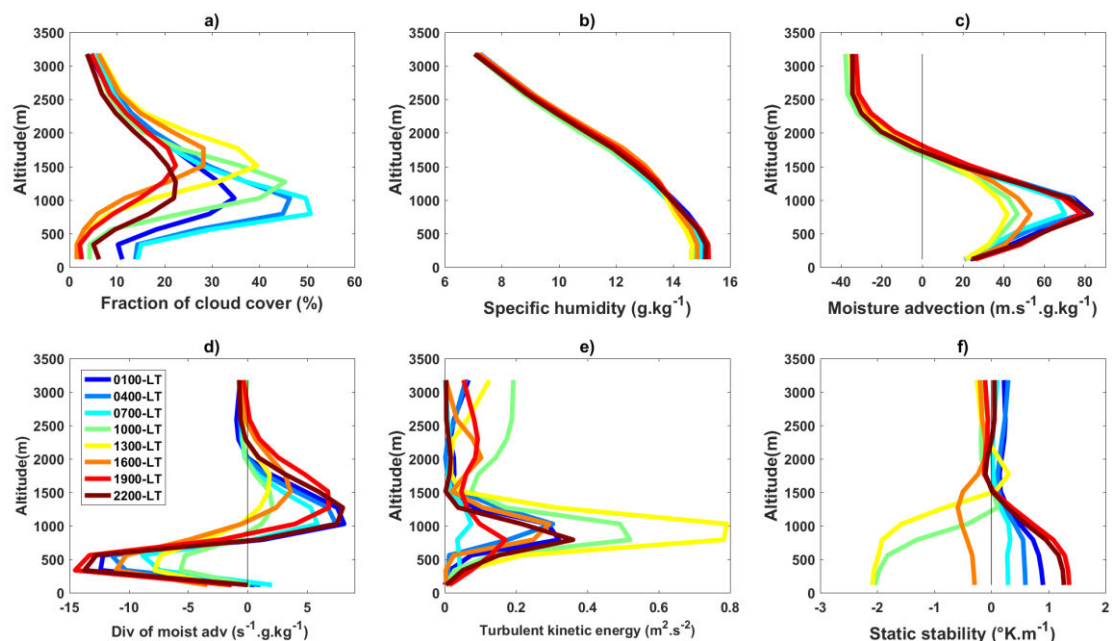
874



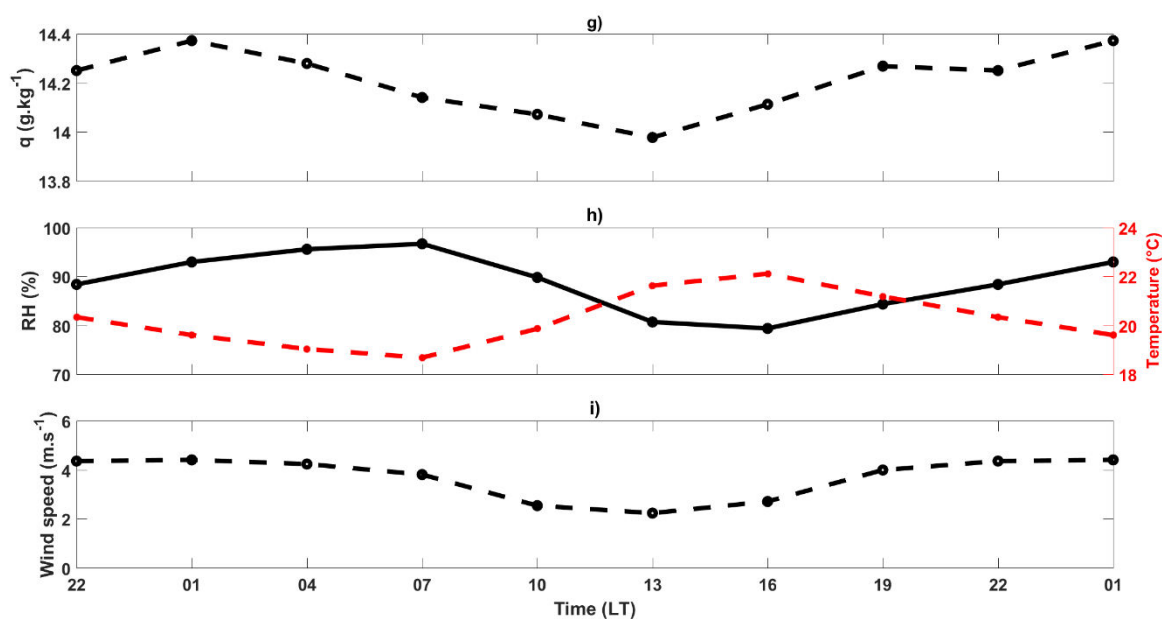
875

876 **Fig. 4** Mean spatial evolution of low clouds cover during the diurnal cycle for ERA5 (panel

877 a), and EECRA (panel b). Black dots on panel a) are pixels with at least 80% of low
878 cloud fraction at 07LT. Triangles (panel b) indicates EECRA stations. For EECRA,
879 only stations (18) recording at least 25% of the data for the JJAS seasons over the 39-
880 year EECRA observation period have been used. Time series (panel c) of total column
881 water vapor (TWV, blue line) and total column cloud liquid water content (LWP, red
882 line) within the green box. Only ERA5 pixels the closest to EECRA stations (**Fig 1**) are
883 considered for times series computation.

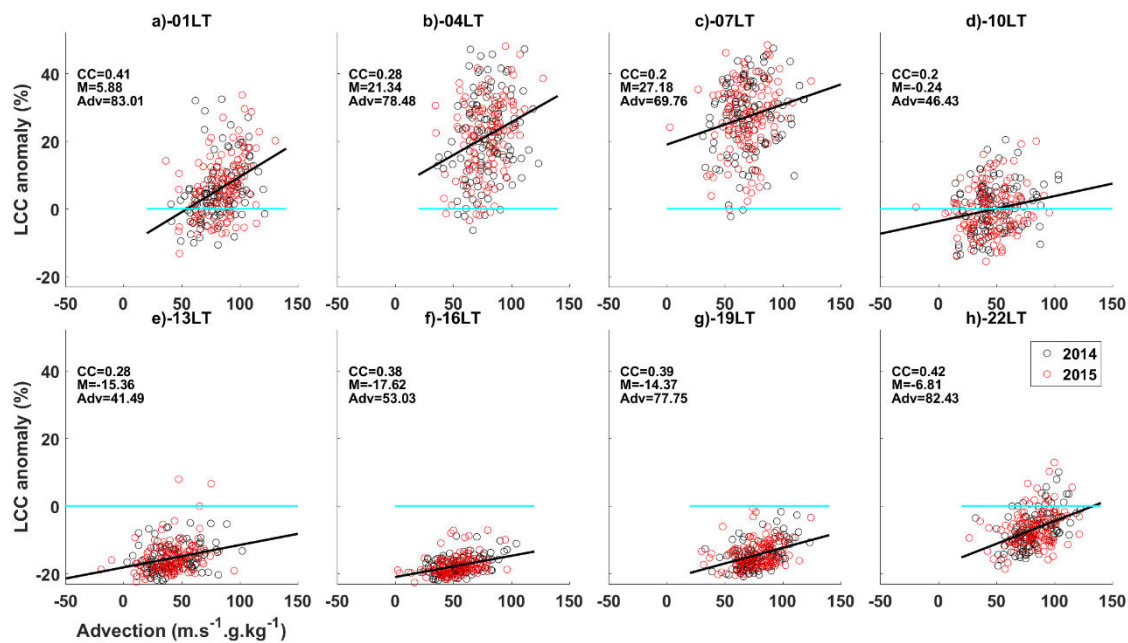


891



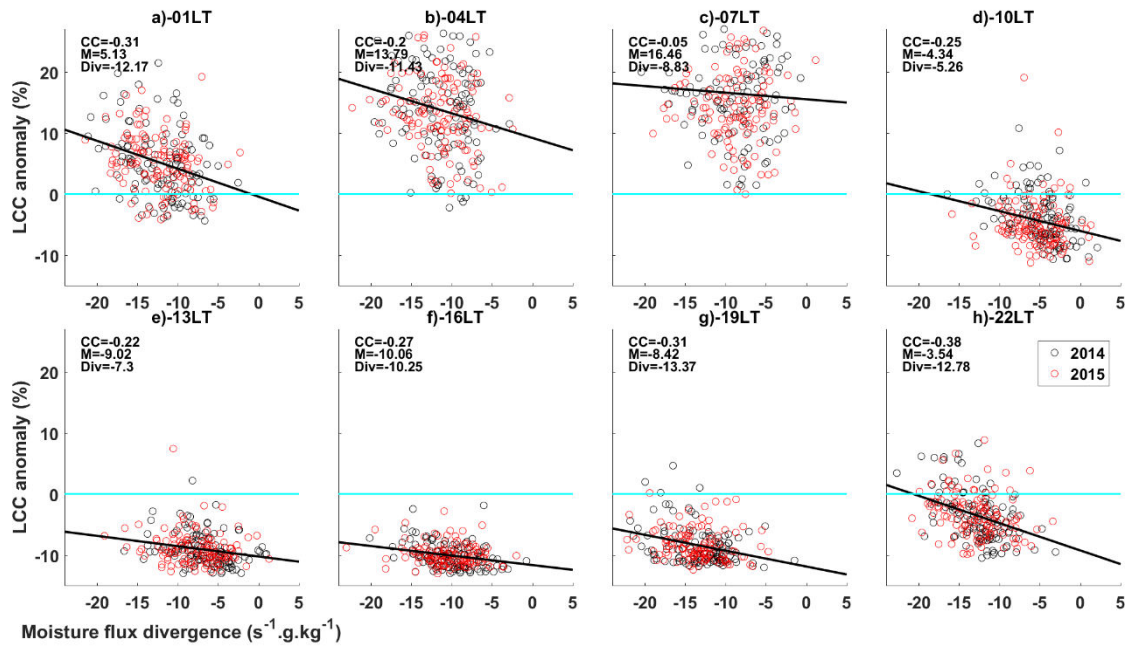
892

893 **Fig. 6** ERA5 Three-hourly vertical profiles from ground level of (a) cloud fraction (%), (b)
 894 specific humidity, (c) moisture advection, (d) divergence of moisture advection, (e)
 895 turbulent kinetic energy, and (f) static stability. Time series of g) specific humidity, h)
 896 relative humidity (black line) and temperature (red line) and, i) horizontal wind speed at
 897 925 hPa i.e about 790m from ground level. Spatial averages are made considering land-
 898 only pixels which record at least 80% of low cloud at 07LT



899

900 **Fig. 7** Scatter plot between low level cloud fraction anomaly and moisture advection at 925
 901 hPa during the diurnal cycle. The scatter plot is obtained by averaging land only pixels
 902 which record at least 80% in low cloud fraction at 07LT within the box 6°S-5°N/8°E-
 903 15°E for the period 2014-2015. For each time slot (01,04,07,10,13,16, 19 & 22LT), the
 904 mean advection (Adv) and the mean low cloud cover anomaly (M) and correlation
 905 coefficient (CC) are computed. The regression line between the two variables is
 906 represented in black, and the reference line ($y=0$) is in green



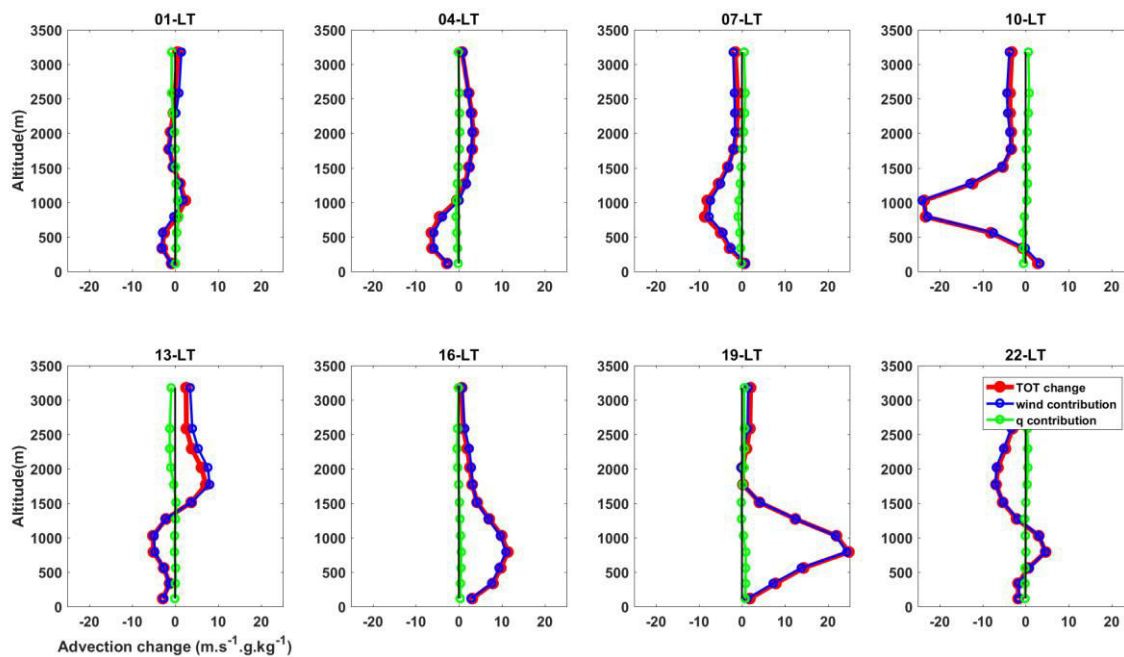
907

908

909 **Fig. 8** Same as fig 7 but between low cloud fraction anomaly and moisture divergence at 950

910 hPa. For each time slot, Div denotes the mean divergence. Negative (positive) values of

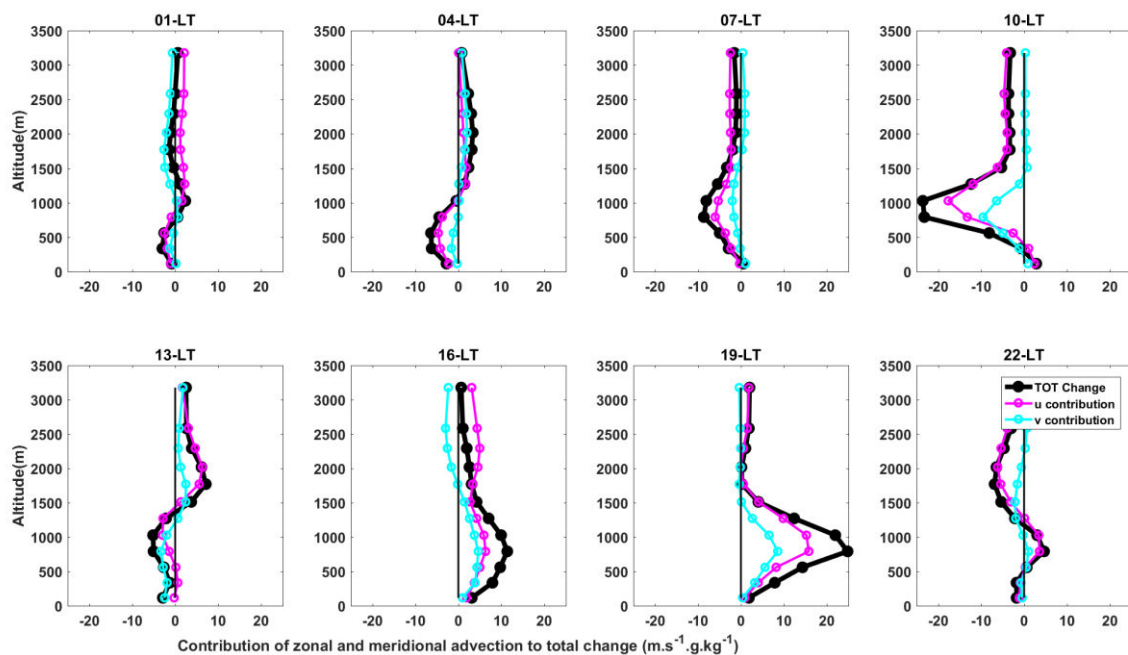
911 divergence expressed moisture inflow (outflow)



912

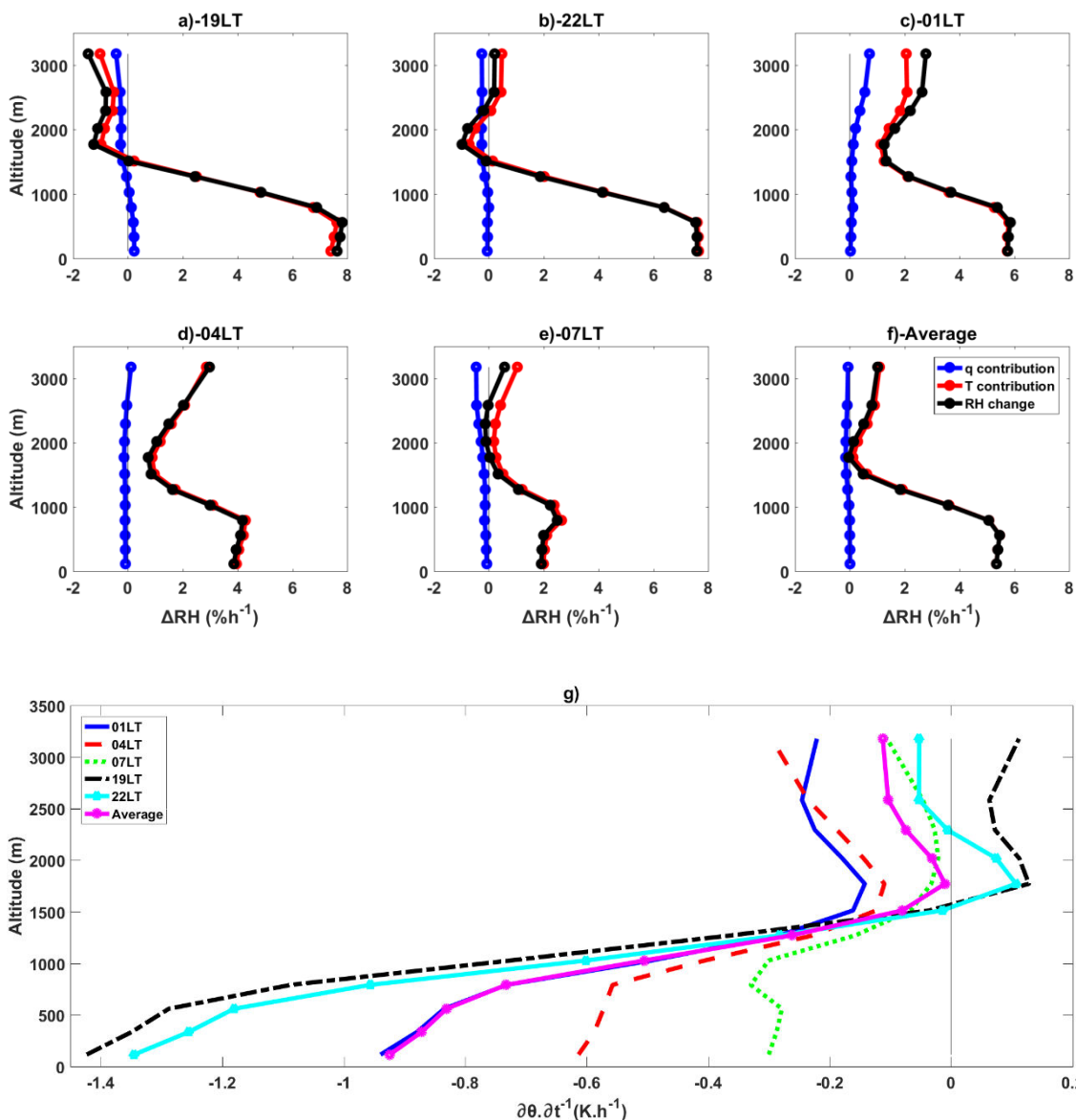
913 **Fig. 9** ERA5 Three-hourly vertical profiles of wind (blue line) and specific humidity (green
 914 line) mean contribution to total advection change (red) from the ground level (pressure
 915 <1000) averaged over 6°S-5°N/8°E-15°E for the period 2014-2015. Only land pixels
 916 with at least 80% of cloud fraction at 07LT are considered for spatial average

917



918

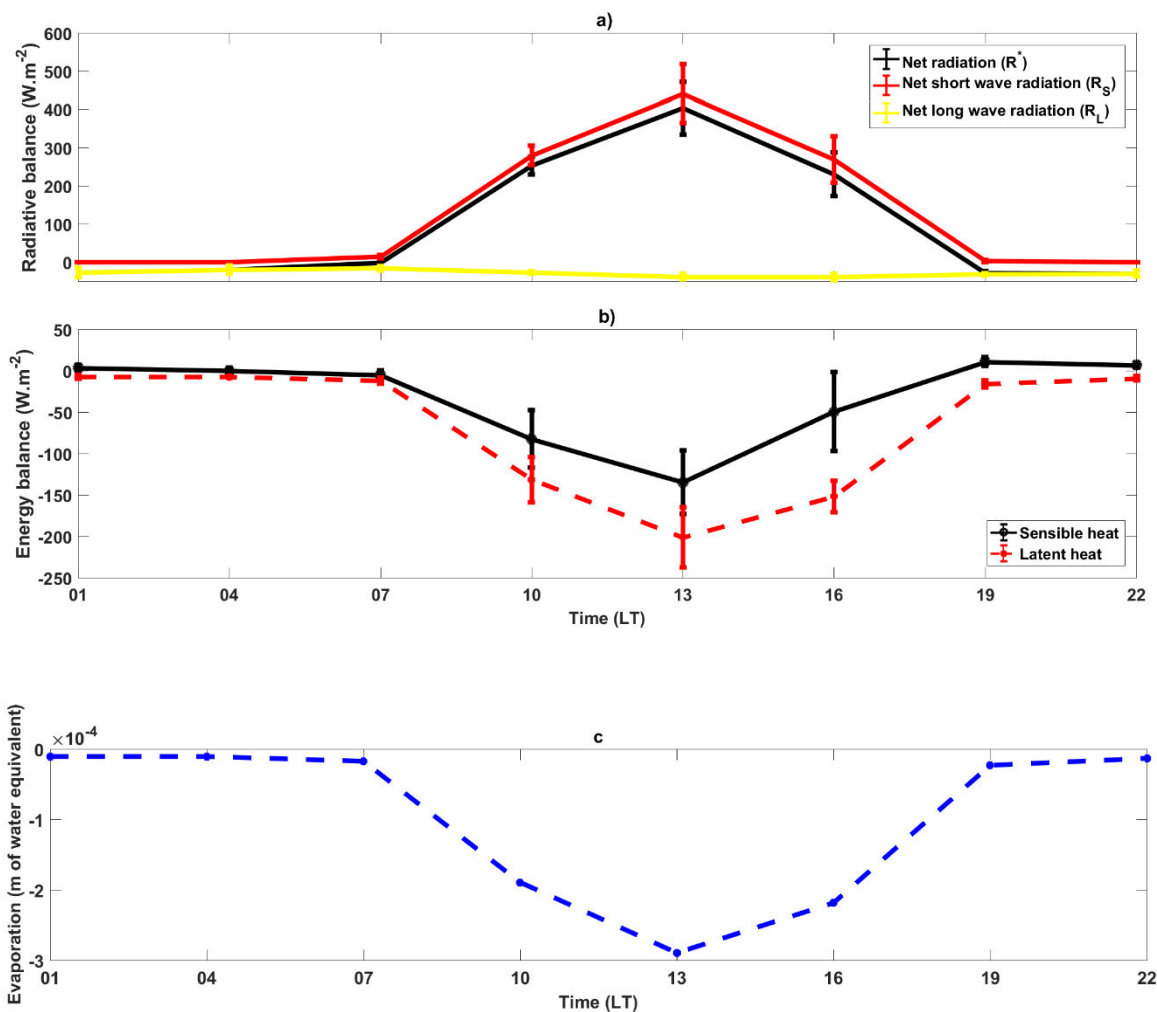
919 **Fig. 10** ERA5 Three-hourly vertical profiles of zonal (magenta) and meridional (cyan) wind
 920 contribution to total advection change (black) from the ground level (pressure <1000)
 921 within 6°S-5°N/8°E-15°E for the period 2014-2015. Only land pixels with at least 80%
 922 of low cloud fraction at 07LT are considered for spatial average



923

924

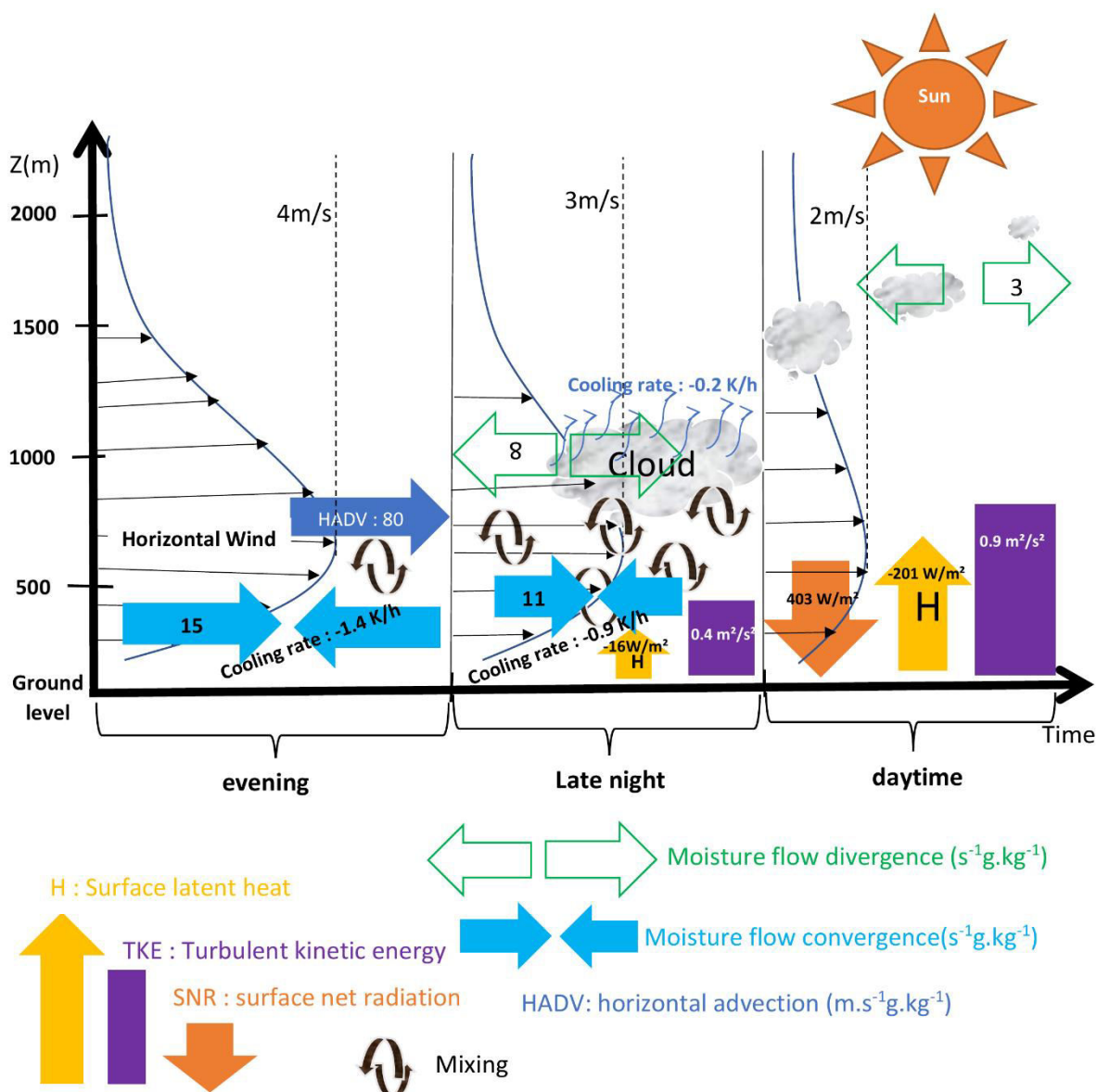
925 **Fig. 11** a-e) ERA5 vertical profiles of specific humidity (q) and temperature (T) contribution
 926 to relative humidity (RH) changes from early evening to early morning (19, 22, 01, 04,
 927 and 07LT). f) average for the five time slots. g) cooling rate from early evening to early
 928 morning (19, 22, 01, 04, and 07LT). The magenta line is the average of the 5 time-slots.
 929 Calculations are made from ground level (pressure < 1000hPa) considering land only
 930 pixels with at least 80% of low cloud fraction at 07LT within 6°S-5°N/8°E-15°E for the
 931 period 2014-2015



932

933

934 **Fig. 12** Diurnal cycle of a) radiative balance (Net radiation: R^* , surface net shortwave
 935 radiation: R_s , Net long wave radiation: R_l), b) energy balance (sensible heat, latent
 936 heat) and c) evaporation within 6°S - 5°N / 8°E - 15°E for the period 2014-2015. Only land
 937 pixels recording at least 80% in low cloud fraction are considered for spatial average.
 938 Error bars indicate the interquartile ranges



939

940 **Fig. 13** Conceptual schematic model illustrating the cloud formation and dissipation processes

941 over WCA along the diurnal cycle. The dark blue lines represent the vertical profiles of

942 the horizontal wind with an indication of its maximum value at evening (19, 22 LT),

943 late night (01, 04, 07 LT) and daytime (10, 13, 16 LT). The dark curled arrows

944 symbolize mixing due to nocturnal turbulence. Maximum values for the contribution of

945 each process are given. Each value is obtained from ERA5 within $6^{\circ}S-5^{\circ}N/8^{\circ}E-15^{\circ}E$

946 for the period 2014-2015

947

948 **Declarations**

949 **Funding :** no funding

950 **Conflicts of interest:** The authors declare that they have no conflicts of interest.

951 **Data availability:** The data used in this study are available on ECMWF website

952 (<https://cds.climate.copernicus.eu/cdsapp#!/dataset>) for ERA5 reanalysis.

953 Terra and Aqua data can be found respectively at

954 https://ladsweb.modaps.eosdis.nasa.gov/archive/allData/61/MOD08_D3/ and

955 https://ladsweb.modaps.eosdis.nasa.gov/archive/allData/61/MYD08_D3/ and EECRA data

956 can be downloaded via <https://rda.ucar.edu/datasets/ds292.2/index.html#!sfol-wl->

957 [/data/ds292.2](https://rda.ucar.edu/datasets/ds292.2/index.html#!sfol-wl-/data/ds292.2)

958

959

960 **Code availability:** All the computations have been made using matlab software. The
961 corresponding code that supports the findings of this study are available upon request from
962 the corresponding author.

963

964 **Ethics approval:** Not applicable

965 **Consent to participate:** Not applicable

966 **Consent to publication:** Not applicable